Chemical Science

ROYAL SOCIETY OF CHEMISTRY

REVIEW

View Article Online
View Journal | View Issue

Cite this: *Chem. Sci.*, 2026, **17**, 8432

Atomic-level engineering of single-atom catalysts for selective C–C coupling in CO_2 hydrogenation to ethanol

Wenyu Zheng,†[a] Yiming Liu,†[b] Xiaohai Zhang,†[c] Shengjie Bai, *[ae] Aobing Li,[d] Kelun Jiang,[a] Feng Wang, [a] Ya Liu, *[a] Yubin Chen [a] and Shaohua Shen [a]

The selective hydrogenation of CO_2 to ethanol represents a pivotal route for sustainable carbon utilization and renewable fuel production, yet its efficiency is fundamentally constrained by the C–C coupling step, which plays the pivotal, rate- and selectivity-determining role in this reaction. Single-atom catalysts (SACs) have emerged as transformative platforms for addressing this challenge, offering atomic-level control over active site geometry, electronic structure, and intermediate stabilization. This review comprehensively examines the design principles and mechanistic insights underlying SACs for selective CO_2-to-ethanol conversion, with emphasis on atomic-scale engineering strategies that enhance C–C coupling while suppressing competing pathways. We discuss how tailored coordination environments, metal–support interactions, and defect engineering (*e.g.*, oxygen vacancies) modulate the adsorption energetics of key intermediates (*CO, *CH_x, and *CH_xO) and transition states to favor ethanol formation. Advanced characterization and computational studies indicate that ternary interfacial structures, which consist of isolated metal sites, defect sites, and support cations, function as minimal functional units to optimize pathway selectivity. Furthermore, we highlight emerging strategies for enhancing SAC stability under practical conditions and address scalability challenges through advanced synthesis techniques like atomic layer deposition. Distinct from prior reviews, this review, by centering on atomic-level design principles and their direct impact on C–C coupling selectivity, provides a roadmap for developing high-performance SACs that achieve unprecedented ethanol selectivity and activity, paving the way toward industrial-scale CO_2 valorization.

Received 27th February 2026
Accepted 27th March 2026

DOI: 10.1039/d6sc01691j

rsc.li/chemical-science

1. Introduction

The conversion of carbon dioxide (CO_2) into value-added chemicals represents a central pillar of strategies aimed at closing the anthropogenic carbon cycle and achieving net-zero emissions.[1–4] Among various CO_2 conversion routes, the catalytic hydrogenation to ethanol represents a particularly compelling approach, offering simultaneous carbon valorization and synthesis of a high-energy-density liquid fuel compatible with existing infrastructure.[5–8] Traditional ethanol production predominantly relies on fossil-derived feedstocks or biomass fermentation, both of which are constrained by feedstock competition, land use pressures, and elevated carbon footprints.[9] CO_2 hydrogenation to ethanol thus represents a promising route to integrate renewable H_2 with anthropogenic carbon sources, offering potential pathways toward a closed carbon cycle and reduced reliance on fossil resources.[1,7,10,11]

The mechanistic complexity of CO_2 hydrogenation to ethanol fundamentally distinguishes it from C_1 product synthesis pathways.[1] Methanol formation proceeds through sequential hydrogenation of the carbon–oxygen double bond, a thermodynamically favourable process with relatively modest kinetic barriers.[12–15] In contrast, ethanol synthesis necessitates C–C bond formation, typically *via* coupling of adsorbed *CO and *CH_x intermediates (*CO + *CH_x → *CH_xCO), which imposes stringent requirements on catalyst active sites.[16] This critical step demands precise orchestration of intermediate adsorption geometries, electronic charge redistribution, and competitive reaction pathway suppression.[17,18] The C_1-to-C_2 transition therefore constitutes the central challenge in CO_2 valorization, with elucidation of C–C coupling mechanisms and selectivity control principles holding profound implications for rational catalyst design.[19]

[a]*International Research Center for Renewable Energy, State Key Laboratory of Multiphase Flow in Power Engineering, Xi'an Jiaotong University, Shaanxi 710049, China. E-mail: shjbai@mail.xjtu.edu.cn*

[b]*Queen Mary University of London Engineering School, Northwestern Polytechnical University, Xi'an 710129, China*

[c]*PetroChina Shenzhen New Energy Research Institute, Shenzhen, Guangdong 518000, China*

[d]*China University of Petroleum (Beijing), Changping District, Beijing, 102249, China*

[e]*Sichuan Digital Economy Industry Development Research Institute, Chengdu, Sichuan, China*

† These authors contributed equally to this work.

Single-atom catalysts (SACs) have emerged as a transformative class of heterogeneous catalysts, exhibiting maximized atomic utilization and unique active site electronic structures that can be precisely tailored through support selection, coordination environment, and metal–support interactions.[19,20] Atomically dispersed metal centres offer well-defined coordination geometries that enable atomic-level control of intermediate binding energies and elementary step energetics, thereby modulating the competitive reaction pathways that dictate selectivity toward ethanol and other higher alcohols.[21] Recent work has demonstrated that SACs can effectively facilitate CO_2 activation, promote *CO formation, and enhance C–C coupling efficiency while suppressing competing pathways such as CO over-hydrogenation and methane formation.[22] Moreover, advanced SAC designs such as cooperative dual single-atom systems and tailored metal heteroatoms supported on defect-rich or electronically modulated supports have shown improved ethanol selectivity and catalytic efficiency, underscoring the importance of active site synergy and electronic regulation in optimizing C_2 product formation. For example, cooperative Ni/Cu SACs have been reported to facilitate *CO coupling and subsequent hydrogenation to ethanol, illustrating how intentional pairing of active centres can modulate reaction pathways at the atomic scale.[23,24] In addition to active site engineering, recent reviews and mechanistic studies have emphasized the critical influence of promoters, support properties (*e.g.*, oxygen vacancies and acid–base functionality), and reaction conditions in balancing elementary reaction steps such as CO_2 activation, hydrogenation, and C–C coupling.[25–28] These coordination and support properties profoundly impact the formation rates of key intermediates and the overall selectivity landscape.

This review synthesizes recent advances in atomic-level engineering of SACs for selective CO_2 hydrogenation to ethanol (Fig. 1). We first dissect the thermodynamic and kinetic features of competing reaction pathways (CO-, formate-, and methoxy-mediated routes) and clarify how SACs rewire pathway selectivity (Section 2). Subsequently, we elaborate on the core principles of SAC atomic-level engineering, which encompass electronic structure modulation, geometric optimization of active sites, and stabilization strategies to mitigate deactivation (Section 3), integrating insights from *operando* characterization and density functional theory (DFT) calculations. Emerging frontiers, including advanced synthesis techniques, integration with renewable H_2 infrastructure, and reactor engineering for industrial scalability, are then discussed (Section 4). Finally, we outline critical challenges and future directions for advancing SAC technologies toward practical implementation (Section 5). This review aims to bridge fundamental catalysis science with applied materials engineering, providing a holistic framework for designing high-performance SACs that unlock the full potential of CO_2 hydrogenation to ethanol as a sustainable carbon valorization technology.

2. Thermodynamics and mechanistic insights into CO_2-to-ethanol conversion over SACs

Selective CO_2 hydrogenation to ethanol is governed by competing reaction pathways in which C–C coupling is both kinetically demanding and thermodynamically disfavoured; SACs enable atomic-scale control of adsorption, charge transfer and site geometry to reconstruct path probabilities toward C_2 formation.

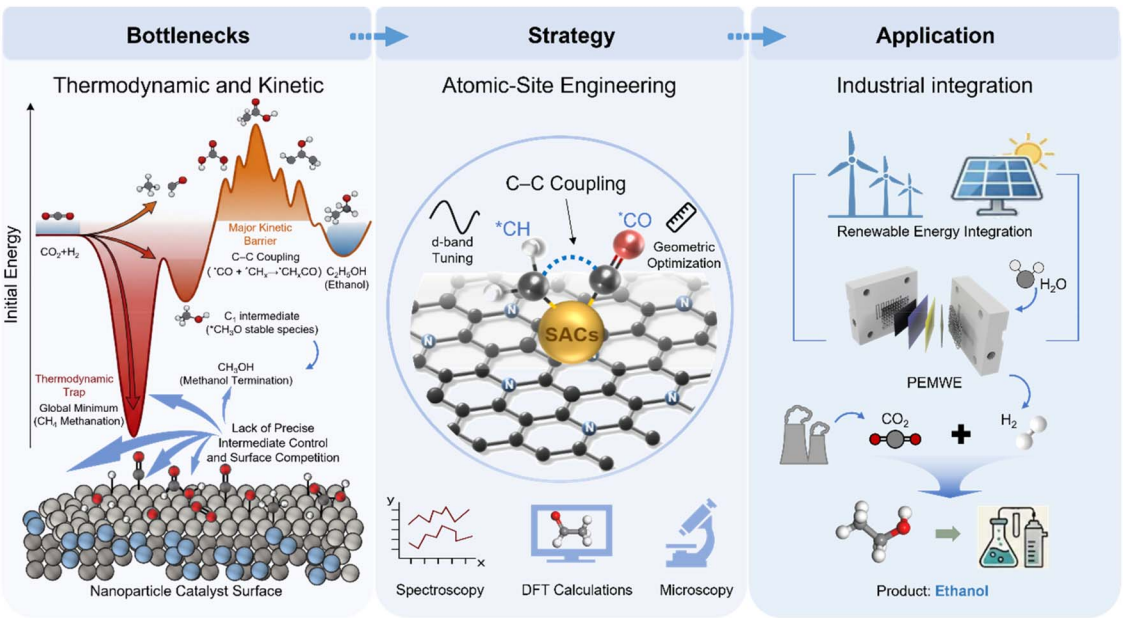

Fig. 1 Schematic illustration of the bottlenecks, strategies, and applications of atomic-level engineering for selective C–C coupling in CO_2 hydrogenation toward ethanol synthesis.

2.1 Competing reaction pathways and the strategic role of SACs

The selective hydrogenation of CO_2 to ethanol is inherently constrained by a complex network of competing reaction pathways, where the thermodynamically disfavoured and kinetically demanding C–C coupling step must outcompete dominant C_1 termination routes (methanation and methanol synthesis) and side reactions (reverse water–gas shift, RWGS). As validated by combined DFT calculations and *operando* characterization techniques (*e.g.*, *in situ* diffuse reflectance infrared Fourier transform spectroscopy, DRIFTS), three principal mechanistic pathways govern product distribution: the CO-mediated route, formate-mediated route, and methoxy-mediated route (Fig. 2).[29,30] A unifying feature across all pathways is the requirement for $*CH_x$ intermediates (x = 1–3) to undergo coupling with carbon-containing species (*CO, *HCOO, and $*CH_xO$) to initiate C_2 formation, making the stabilization of these key intermediates and modulation of their coupling kinetics the central design criterion for selective catalysis. Table 1 delineates the distinct mechanistic features, key intermediates, and rate-determining steps inherent to the CO-, formate-, and methoxy-mediated pathways. This systematic comparison is instrumental for deciphering the origins of pathway selectivity and establishing structure–activity relationships essential for targeted catalyst engineering.

The CO-mediated pathway stands as the most extensively validated and kinetically favourable route for ethanol synthesis.[29,31] This pathway initiates with CO_2 activation to *COOH, whose dissociation yields *CO—the pivotal C1 intermediate. Subsequent hydrogenation of *CO generates $*CH_x$ species, whose coupling with *CO or $*CH_xO$ yields C_2 precursors ($*CH_xCO$) that proceed to ethanol *via* sequential hydrogenation. Computational studies on χ-Fe_5C_2 (510) surfaces quantify this kinetic advantage: the activation barrier for $*CH_2O$ + $*CH_2$ coupling ($\approx$0.52 eV) is substantially lower than that of C_1 termination pathways (>0.7 eV) or alternative C_2 formation routes.[32] *Operando* DRIFTS investigations on Cs–CuFeZn catalysts further confirm the pathway's relevance, identifying adsorbed acetaldehyde and ethoxy intermediates as direct products of *CO insertion into $*C_xH_y$ species, formed *via* RWGS-derived CO hydrogenation, while ruling out methanol as a C_2 precursor through methanol steam reforming control experiments.[33]

The formate-mediated pathway proceeds *via* stepwise hydrogenation of CO_2 to *HCOO, $*H_2COO$, and $*CH_3O$ intermediates, with C–C coupling achieved through $*CH_3$ (generated by C–O bond scission) reacting with *CO to form $*CH_3CO$. However, this route suffers from intrinsic thermodynamic bias toward C_1 products, as the high stability of $*CH_3O$ intermediates promotes methanol formation over C–C coupling.[34–36] Limited exceptions have been reported in cobalt-based systems ($CoAlO_x$ and $Co_{0.52}Ni_{0.48}AlO_x$) and Cu/Cs/ZnO catalysts, where *operando* FTIR spectroscopy and DFT-KMC simulations confirm $*CH_x$ insertion into *HCOO to form acetate ($*CH_3COO$) or *OHCCHO intermediates.[37,38] Notably, Cs promotion in Cu/Cs/ZnO facilitates *HCOO dissociation to *CHO, a critical precursor for C–C coupling, yet the pathway's overall selectivity remains inferior to the CO-mediated route in conventional catalytic systems.[39]

The methoxy-mediated pathway, although less prevalent, offers a mechanistically distinct route for CO_2 hydrogenation to ethanol, beginning with the formation of methoxy ($*CH_3O$) intermediates. Studies on Pt/Co_3O_4 and Cu@Na-Beta catalysts show that methoxy groups can be protonated, often with water assistance, or directly split to produce methyl ($*CH_3$) species, which then couple with *CO or activated CO_2 to yield ethanol.[40] DFT calculations by Chen *et al.* revealed that electron-rich Pd dimers substantially lower the energy barrier for $*CH_3O$ coupling to −0.3 eV, while single-atom Pd sites present a significantly higher barrier.[41] This highlights the critical role of the local electronic structure and cooperative dual-atom effects. Furthermore, Yang *et al.* found that surface CH_x species (x = 1–3) not only participate in C–C coupling but also regulate catalytic activity and selectivity by influencing surface hydrogen dynamics.[42] Complementary work by Deng's group,

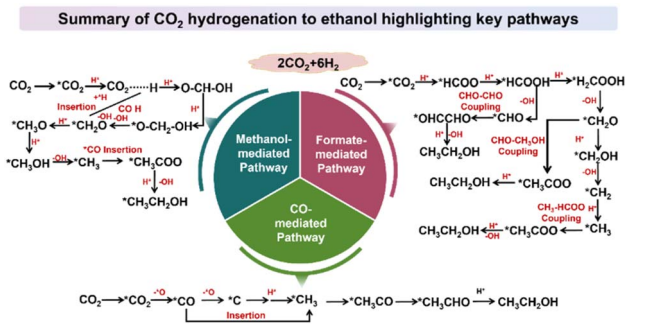

Fig. 2 Three principal mechanistic pathways of CO_2 hydrogenation to ethanol: the CO-mediated route, formate-mediated route, and methoxy-mediated route.

Table 1 Comparative analysis of CO_2 hydrogenation pathways toward ethanol over SACs

Pathway	Key intermediates	C–C coupling mode	Rate-determining step (RDS)	Limitations
CO-mediated	*CO, $*CH_x$, and $*CH_xCO$	*CO + $*CH_x$ → $*CH_xCO$	*CO hydrogenation or $*CH_x$–CO coupling	Requires balanced *CO and $*CH_x$ stabilization
Formate-mediated	*HCOO, $*CH_3O$, $*CH_3$, and $*CH_3CO$	$*CH_3$ + *CO → $*CH_3CO$	C–O bond cleavage of $*CH_3O$ or $*CH_3$ formation	Strong tendency toward methanol formation; poor C–C coupling selectivity
Methoxy-mediated	$*CH_3O$, $*CH_3$, and *CO	$*CH_3$ + *CO → ethanol precursors	$*CH_3O$ dissociation or coupling step	Limited generality

integrating spectroscopy and theory, clarified how axial oxygen coordination at tin centres directs the transformation of *OCHO intermediates to formic acid, emphasizing the importance of the coordination environment in the reaction pathway.[43]

A core mechanistic insight is that efficient C–C coupling requires concurrent stabilization of *CO and *CH_x intermediates in geometries conducive to bond formation. SACs excel in this regard by leveraging coordination-induced charge coupling between isolated metal centres and support defects (*e.g.*, oxygen vacancies).[44,45] This interaction modulates the d-band centre of metal sites and tunes the energy difference between transition states and adsorbed intermediates, directly optimizing intermediate stability at the potential energy surface level. Such atomic-level control suppresses competing pathways (*e.g.*, CO over-hydrogenation and methanation) while promoting C_2 formation, an advantage unattainable with conventional nanoparticulate catalysts.[21,38,46,47]

2.2 Thermodynamic landscape and catalyst design strategies for pathway selectivity

From a macroscopic thermodynamic perspective, the overall free energy landscape of the CO_2 hydrogenation system typically shows a trend towards more hydrogenated, hydrogen-saturated products (such as methane), making methanation thermodynamically advantageous. Although methanol synthesis can be achieved through appropriate catalysts and reaction conditions in terms of kinetics, it is generally in an unstable state and is limited by reaction conditions.[48] Therefore, the selective generation of ethanol requires intentionally deviating from the thermodynamically spontaneous and kinetically favored C_1 pathway. This objective is achievable only *via* precision catalyst engineering that balances intermediate stabilization and C–C coupling promotion. This deviation is achievable through precision catalyst engineering that leverages geometric structural reconfiguration and electronic state modulation to stabilize C_1 intermediates while simultaneously facilitating their C–C coupling (Fig. 3a).[49,50]

Conventional nanoparticulate catalytic systems attempt to enhance C–C coupling probability through elevated metal loadings.[51] However, such approaches fail to regulate the surface residence time of individual intermediates, leaving the system prone to excessive hydrogen coverage, which thermodynamically favors C_1 products.[52] In stark contrast, SAC architectures exhibit atomic-scale electronic localization, enabling precise control over the adsorption energetics of *CO, *CH_x, and *CH_xO intermediates within extended M–O–M′ coordination environments (Fig. 3b). This tunability maintains intermediates in an optimal adsorption regime: strong enough to prevent premature desorption but weak enough to avoid irreversible binding or displacement by competitive H_2 adsorption.[21,44]

The exceptional ethanol selectivity of SACs originates from the effective suppression of methanation and methanolization pathways.[53–56] The transformation of CO_2 to ethanol *via* SACs can thus be conceptualized as a competitive pathway probability reconstruction process driven by electronic structure engineering. This reconstruction aligns with the core requirement of selective C_2 synthesis, which is overcoming the intrinsic thermodynamic and kinetic biases toward C_1 products.[53,57–59] It also establishes the foundational logic for subsequent atomic-level engineering strategies (Section 3), where electronic and geometric modulation of SAC active sites is tailored to further optimize this pathway selectivity.[60,61]

3. Atomic-level engineering of SACs: design principles and recent advances

The rational design of single-atom catalysts for selective CO_2-to-ethanol conversion requires fundamental understanding of

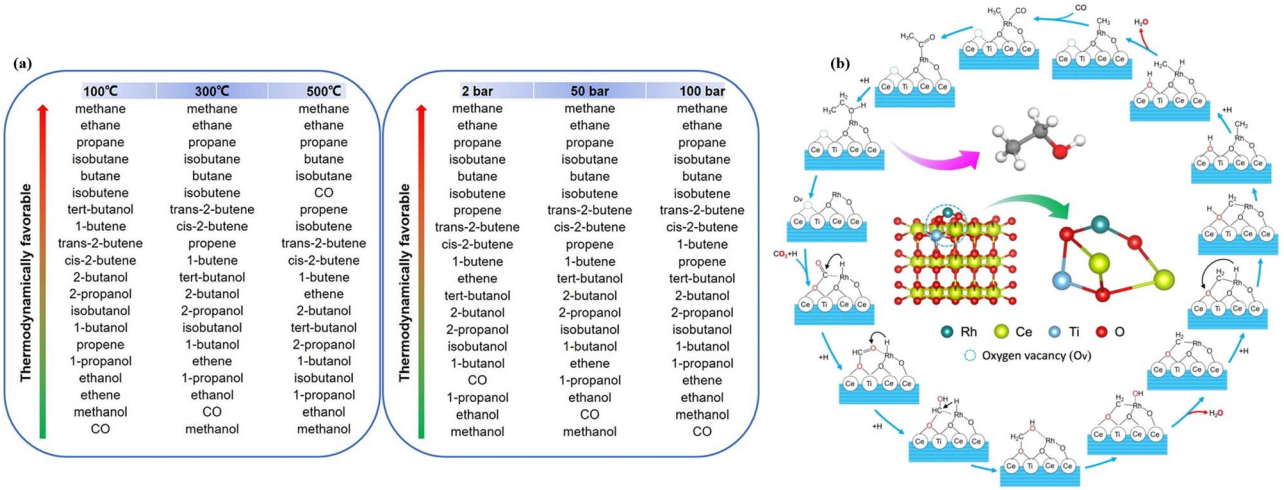

Fig. 3 Thermodynamic effects of reaction conditions and the catalytic cycle for CO_2 hydrogenation to ethanol. (a) Effects of temperature and pressure on the thermodynamics of various products in CO_2 hydrogenation; reproduced with permission.[62] Copyright 2022, American Chemical Society. (b) Illustration of the catalytic cycle of ethanol formation from CO_2 hydrogenation on the $Rh_1/CeTiO_x$ catalyst. The insets show the structure of the $Rh_1/CeTiO_x$ catalyst; reproduced with permission.[44] Copyright 2022, John Wiley and Sons.

Table 2 Representative performances of SACs for CO_2 hydrogenation to ethanol

No.	Catalyst	pH_2/pCO_2 (bar bar^{-1})	Temperature (°C)	Pressure (MPa)	TOF (h^{-1})	Selectivity (%)	STY ($g_{EtOH}\ g_{cat}^{-1}\ h^{-1}$)	Stability/time (h)	Ref.
1	Ir_1/In_2O_3	5 : 1	200	6	481.2	99.7	0.046	5 h (Time)	65
2	$Rh_1/CeTiO_x$	3 : 1	250	3	493.1	99.1	0.265	5 cycles	44
3	Rh/CN	3 : 1	250	3	—	91.3	—	5 h (Time)	66
4	Rh/CNP	3 : 1	250	3	420.7	81.8	—	5 h (Time)	66
5	$Rh–N_3P_1$	3 : 1	250	3	420	81.8	3.6	5 h (Time)	66
6	Pd/Fe_3O_4	4 : 1	300	0.1	—	97.5	19.0	—	67
7	Pd_2/CeO_2	3 : 1	240	3	211.7	99.2	45.6	—	68
8	Pt/Co_3O_4	3 : 1	200	8	—	82.5	0.013	—	69
9	$Cu–N_4$ SAC	3 : 1	150	3.2	—	95.5	—	3 h (Time)	70
10	$Pd_2Ce@Si_{16}$	3 : 1	250	3	—	98.7	11.6	60 h	41
11	Zr_{12}-bpdc-CuCs	3 : 1	100	2	—	99	4.05	3 cycles	71
12	Au_1/TiO_2	3 : 1	200	6	—	99	0.954	6 cycles	72
13	Cu	—	190	0.1	—	84	1.0×10^{-7}	—	73
14	Cu/ZrO_2	3 : 1	180	3	2.89	100	—	—	74
15	Cu/ZnO	3 : 1	170	3	—	99.1	—	—	75

how atomic-level structural features govern catalytic performance.[21,63,64] This section systematically examines three interconnected design pillars: (1) electronic structure modulation through coordination environment engineering to control intermediate binding energies and transition state stabilization, (2) geometric optimization of active site configurations to facilitate C–C coupling while suppressing competing pathways, and (3) stability enhancement strategies addressing deactivation mechanisms including sintering, carbon deposition, and metal–support interactions. By integrating insights from advanced characterization techniques and computational modelling, we establish structure–performance relationships that guide the development of robust and selective SAC systems for practical CO_2 utilization (Table 2).

3.1 Electronic structure modulation and coordination environment engineering

The transformative potential of SACs derives from their capacity to achieve directional regulation of reaction potential energy surfaces at the intermediate level by controlling the local electronic structure of isolated metal centres.[76] The binding energy is determined by the electronic structure of the active centre, which is controlled by its local coordination environment.[77] Extensive theoretical and spectroscopic investigations have demonstrated that the relative energy barriers governing different intermediates (*CO, $*CH_x$, $*CH_xO$, and $*CH_3CO$) are not uniformly distributed across active metal surfaces but rather exhibit pronounced dependence on the coordination environment of the single metal centre and the degree of charge polarization at surrounding defect sites such as S vacancies (S_v), O vacancies (O_v), and N vacancies (N_v).[78,79]

Hu *et al.* demonstrated that sulfur vacancy-rich MoS_2 serves as an efficient catalyst for CO_2 hydrogenation to methanol by tailoring the local electronic structure through defect engineering (Fig. 4a).[80] S_v provide unsaturated sites that enhance CO_2 activation and stabilize intermediates, promoting electron transfer and lowering reaction barriers (Fig. 4b). Their combined experimental and computational analysis highlights how atomic-level coordination modulation can markedly improve catalyst activity and selectivity in CO_2 conversion. A critical mechanistic insight emerging from recent studies indicates that the key structural unit capable of generating bias toward C_2 product pathways in CO_2 hydrogenation is a ternary interface composed of an "isolated metal-defect site (such as O_v)-carrier cation" assembly, rather than the isolated metal atom itself.[65] This ternary interfacial configuration fundamentally distinguishes SACs from conventional nanoparticulate catalysts, as it enables atomic-level control over electronic charge redistribution and intermediate stabilization.[83–85] On reducible oxide supports such as In_2O_3, CeO_2, and TiO_2, isolated metal sites and adjacent oxygen vacancies synergistically form highly polarized local coordination environments that facilitate CO_2 activation. O_v in the support play a crucial role in the catalytic performance of CO_2 hydrogenation.[86] Electrons are injected into the lowest unoccupied molecular orbital of CO_2, thereby achieving a bent adsorption configuration characteristic of activated CO_2 excited states.[87,88]

The critical role of metal–adsorbent interactions has been unequivocally demonstrated in Pt single-atom systems. In the Pt_1/FeO_x catalytic architecture, joint XAS/XPS and DFT analyses confirm that Pt_1 exists in a partially positive valence state on iron oxide surfaces, resulting from local charge redistribution driven by electron back-donation from Fe^{2+} to Pt.[89] This local electronic structure modification significantly affects the adsorption mode and activation energy of *CO intermediates, indicating that electron transfer can be optimized through carrier defect engineering.[90] Comprehensive analyses reveal that in $Fe_3O_4(001)$ single-atom systems (Fig. 4d), CO adsorption energies at different metal single-atom sites exhibit a comparable trend relationship with the proximity of d-electron states to the Fermi level (E_F), with d-band centre deviation directly regulated by local coordination environments (Fig. 4c).[81,82] The

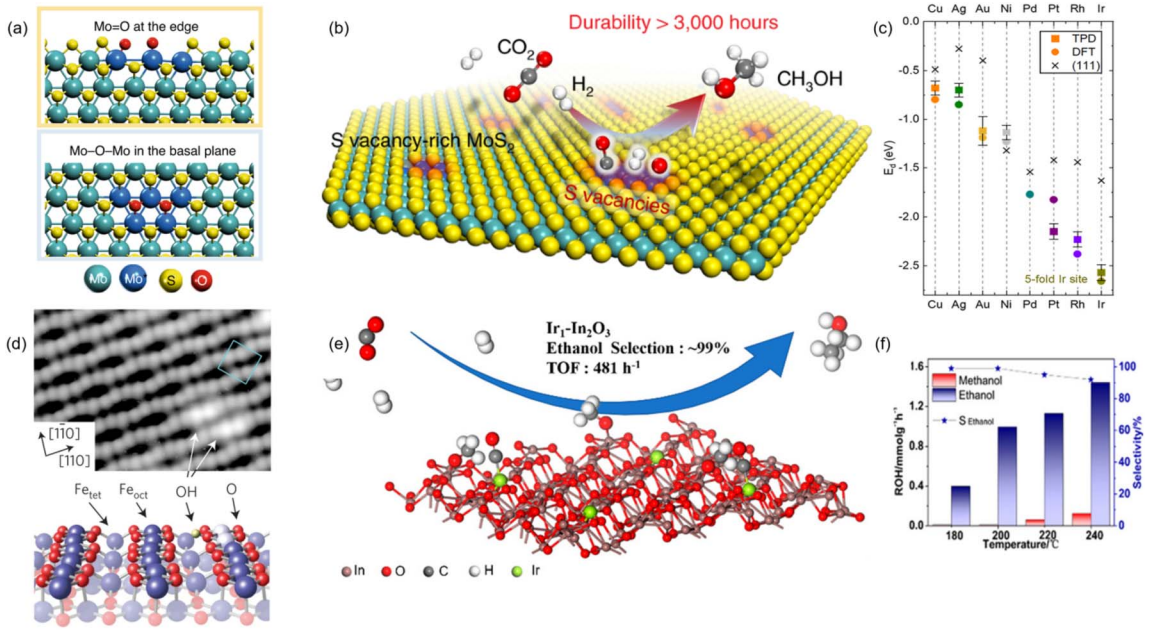

Fig. 4 Structural characterization, catalytic performance, and electronic structure correlations of catalysts for CO_2 hydrogenation to ethanol. (a) DFT-calculated structures of the adsorption of oxygen at the edge (top) and in-plane (bottom) S_v over S_v-rich MoS_2, (b) schematic diagram of in-plane sulfur vacancies driving the selective hydrogenation of CO_2; reproduced with permission.[80] Copyright 2021, Springer Nature. (c) The CO adsorption energy of metal monatomic species on the Fe_3O_4(001) surface and its relationship with the d-band centre; reproduced with permission.[81] Copyright 2022, American Chemical Society. (d) The Fe_3O_4(001) surface.; reproduced with permission.[82] Copyright 2013, Springer Nature. (e) Highly selective hydrogenation of CO_2 to ethanol *via* a designed bifunctional Ir_1–In_2O_3 SAC and (f) the ethanol selectivity over Ir_1–In_2O_3: the effect of temperature in 3.0 mL of H_2O, initial pressure 6.0 MPa (H_2/CO_2 = 5 : 1), catalyst 20 mg; reproduced with permission.[65] Copyright 2020, American Chemical Society.

Ir_1–In_2O_3 system exemplifies this design principle with exceptional clarity (Fig. 4e).[65] The Ir–O_v–In^{3+} interface formed when Ir atoms are anchored proximal to oxygen vacancies reduces the *CH_3CO transition state energy by approximately 0.4–0.5 eV relative to metallic Ir surfaces, achieving ethanol selectivity exceeding 99% at 473 K and 60 bar (Fig. 4f). This performance on Ir_1–In_2O_3 quantitatively demonstrates that reaction pathway selectivity can be precisely engineered through local electronic environment control to stabilize specific transition states. Consequently, charge transfer behaviour emerges as a key descriptor for modulating reaction pathways in SAC systems. Iron-based carbide systems can be conceptualized as an extension of this local electronic structure regulation strategy toward selective pathway control. The χ-Fe_5C_2 (510) surface achieves CO insertion within an energy range of approximately 0.4–0.6 eV to form C–C coupling transition states—significantly lower than the energy barriers corresponding to C_1 termination channels (>0.7 eV), consistent with the "effective energy window" effect of single-centre electronic structure regulation.[46,47] This phenomenon has been independently verified in atmospheric-pressure CO_2 hydrogenation for long-chain olefin synthesis, where iron carbide introduction stabilizes CO insertion intermediates at lower energy barriers, dramatically increasing the proportion of C_2–C_4 hydrocarbon products.[91]

These convergent research findings establish that SAC superiority does not stem solely from metal dispersion but rather from precise local electronic structure regulation enabled by the "isolated metal-defect site-carrier cation" ternary interface. This enables C–C coupling-related transition states to gain measurable kinetic advantages in free energy space compared to C_1 termination pathways, thereby enhancing C_2 product (ethanol) formation efficiency.[65,92,93] This mechanism has been independently validated across Ir_1–In_2O_3, Pt_1/Fe_3O_4, and Fe_5C_2 (510) systems, establishing SAC as a fundamental catalytic design route that "achieves reaction path selectivity reconstruction through local electronic structure engineering".[76]

3.2 Atomic-level control of C–C coupling *via* coordination engineering

SACs can precisely control the adsorption configuration and electronic structure of intermediates at the atomic scale, thereby simultaneously promoting C–C coupling, demonstrating exceptional potential for CO_2 hydrogenation to C_2 products.[28,96] The Ir_1–In_2O_3 system represents the paradigmatic example of this design principle.[65] In this catalyst architecture, isolated Ir single atoms are anchored proximal to oxygen vacancies (O_v) on In_2O_3, forming an Ir–O_v–In^{3+} ternary interface that achieves dual-functional synergy: Lewis acidic–basic sites on In_2O_3 promote CO_2 activation, while Ir sites stabilize *CO (carbonyl intermediate) adsorption and facilitate C–C coupling reactions with methoxy groups (*OCH_3) on the In_2O_3 surface.[21]

Recent breakthrough studies have demonstrated that the Ir_1–P_x/In_2O_3 catalyst achieves an impressive ethanol yield of 3.33 mmol g^{-1} h^{-1} and a turnover frequency of 914 h^{-1} under

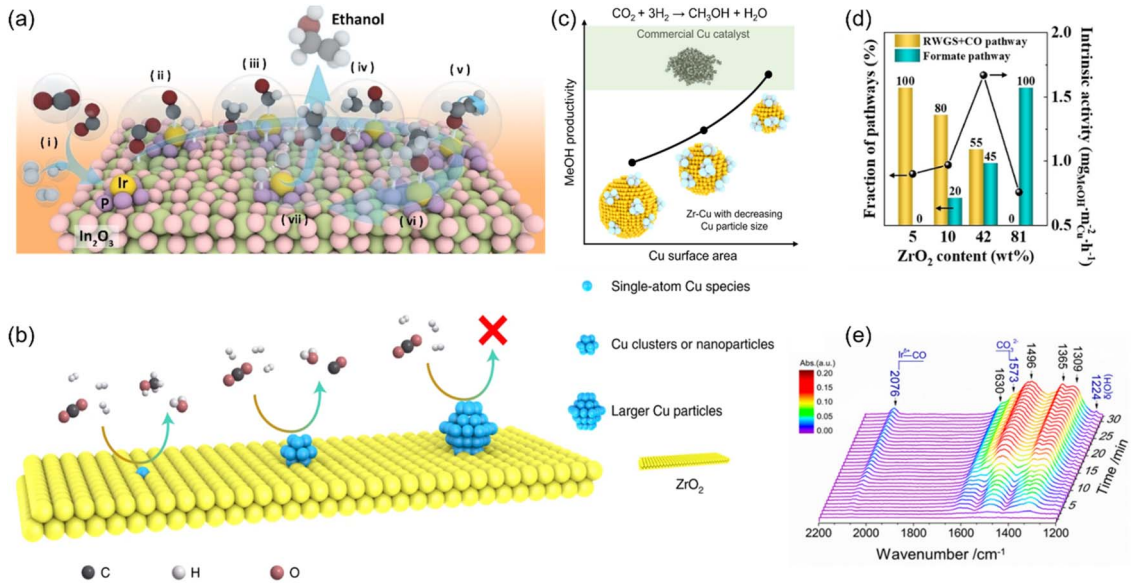

Fig. 5 Catalytic roles of SACs and related catalysts in CO_2 hydrogenation: pathway regulation, C–C coupling promotion, and spectroscopic characterization. (a) Schematic illustration of Ir single atoms precisely anchored on P islands of In_2O_3 nanosheets, highlighting enhanced CO_2 adsorption, C–C coupling, and H_2 dissociation for highly selective ethanol production; reproduced with permission.[21] Copyright 2025, John Wiley and Sons. (b) Schematic diagram for the CO_2 hydrogenation reaction on different types of copper species; reproduced with permission.[74] Copyright 2022, Springer Nature. (c) CO_2 hydrogenation over the inverse Zr–Cu catalyst; reproduced with permission.[94] Copyright 2024, Elsevier. (d) The fraction of reaction pathways and their contributions to methanol selectivity over Cu/Zr–SiO_2 samples with various ZrO_2 content in catalysts; reproduced with permission.[95] Copyright 2023, John Wiley and Sons. (e) *In situ* DRIFTS of CO_2 hydrogenation with the Ir_1–In_2O_3 catalyst after exposure to CO_2 at 200 °C; reproduced with permission.[65] Copyright 2020, American Chemical Society.

moderate conditions, nearly 8 times higher than that of the unmodified Ir_1/In_2O_3 catalyst, with the TOF reaching 2108 h^{-1} at industrially relevant pressure (Fig. 5a).[21] The specific coordination of the Ir centre with P islands not only alters the electronic structure to optimize CO_2 adsorption and C–C coupling ability, but P atoms also exhibit excellent H_2 dissociation ability compared to the Ir single atomic site. These data unequivocally confirm that the Ir–O_v–In^{3+} three-site structure renders the free energy of the *CH_3CO transition state substantially lower than that on metallic Ir particle surfaces, thereby suppressing over-hydrogenation (C_1 pathway) and stabilizing coupling intermediates.

Copper-based single-atom catalysts exhibit tunable C–C coupling behaviour during CO_2 hydrogenation processes and are regarded as important candidates for promoting C–C bond formation.[97,98] As shown in Fig. 5b, compared with clusters/large-particle Cu, by introducing doped atoms with weak M–C interactions (such as introducing Zn, Ag or other metals/atoms with weaker valence states near the Cu lattice or sites), the adsorption strength of *CO can be weakened, promoting the migration and relaxation of adsorbed *CO on the surface/positions, thereby reducing the effective energy barrier for C–C coupling and increasing the yield of C_2 (such as ethanol).[74]

Furthermore, studies on the metal–support interface or the Cu–Zr monomer system derived from MOFs have shown that isolated Cu sites and their adjacent Zr–O coordination units can reconfigure the electronic density distribution at the atomic level, significantly enhancing the activation of CO_2 and stabilizing key intermediates (such as *CO, *HCOO, and *CHO), making the gradual hydrogenation path through intermediates such as CHO more favourable in terms of kinetics (Fig. 5c). At the same time, it also provides favourable charge and geometric foundations for the subsequent *CO–*CH_x coupling.[94] The relevant DFT potential energy profiles indicate that, on certain Zr_1–Cu or Cu/ZrO_2 unit site models (Fig. 5d), the energy barrier required to form C–C precursors (such as *CHO and *CH_2O) is significantly lower than the energy barrier for direct CO_2 dissociation to *CO. This suggests that "moderately stable CO_2 adsorption + enhanced stability of intermediates" is conducive to favouring the generation of C_2 products rather than favouring the thermodynamically more stable C_1 pathway. Although these studies did not specifically analyze the C–C coupling process of C_2 products, their theoretical analyses of *CO adsorption, decomposition pathways, and intermediate stability laid the foundation for designing copper-based solid acid catalytic systems for ethanol production. From the above DFT analyses, coupling reactions (C–C bond formation) in CO_2 hydrogenation to C_2 products proceed through isomerization coupling between partially hydrogenated carbon intermediates (such as *CH_2O or *CH_x) and adsorbed *CO (or *CHO). Therefore, to lower C–C formation barriers, on the one hand, CO adsorption strength must be maintained within appropriate ranges, and on the other hand, partially hydrogenated carbon intermediates must be stabilized to facilitate their entry into coupling transition states.[95,99]

At the experimental level, *operando* spectroscopy and isotope tracing techniques provide compelling evidence for these theoretical frameworks. In the Ir_1–In_2O_3 system, *operando*

DRIFTS detected coexisting spectral bands of carbonyl (*CO) and methoxy (*OCH_3), with spectral intensities positively correlated with ethanol formation rates (Fig. 5e). This unambiguously demonstrates that CO and partially hydrogenated oxygen-containing intermediates coexist on catalyst surfaces and jointly participate in C–C coupling reactions, validating the mechanistic paradigm established through computational studies.[65]

3.3 Stability challenges and mitigation strategies

While SACs demonstrate unique advantages in achieving high selectivity and atomic utilization, their long-term stability under thermal catalytic gas-phase/liquid-phase reaction conditions remains a primary challenge impeding industrial applications.[100] Relevant studies have identified three principal physical and chemical processes driving SAC deactivation: (1) site sintering characterized by single-atom aggregation into metal clusters/nanoparticles, (2) carbon deposition/reconstruction involving SAC site coverage by carbonaceous deposits, thereby reducing reaction rates, and (3) chemical interactions with supports manifesting as structural reconfiguration caused by strong metal–support interactions resulting in anchoring site loss.[81,101–103] These deactivation pathways diminish SAC activity and alter intermediate adsorption configurations, thereby shifting product distribution and selectivity. The construction of single-atom sites represents a promising strategy to enhance the catalytic efficiency of CO_2 conversion, yet maintaining their structural integrity under operating conditions requires sophisticated design strategies.

3.3.1 Site sintering and metal aggregation. The Ir_1–In_2O_3 catalytic system provides specific case studies regarding SAC site sintering phenomena.[65] While exhibiting up to 99.7% ethanol selectivity and relatively high initial conversion rates (TOF ≈ 481 h^{-1}) in initial states, Ir_1–In_2O_3 exhibits severe deactivation when Ir loading increases or during long-term cycling. In particular, when the Ir mass fraction increases from 0.2 wt% to 1.0 wt%, ethanol selectivity drops from 85.3% to 5.7%, with TOF declining nearly to 0 h^{-1}. HAADF-STEM and EXAFS characterization results support these conclusions: excessive Ir leads to local reduction and promotes Ir atom aggregation into Ir_n clusters, ultimately forming 1–2 nm nanoparticles. Simultaneously, In_2O_3 undergoes over-reduction, resulting in increased Ir^0 and metallic bonding, thereby reducing CO and intermediate adsorption properties and C–C coupling capabilities. Therefore, maintaining monodisperse SAC states and avoiding excessive support reduction are key to maintaining high C_2 selectivity.

Another study on Rh-modified CeO_2(111) surfaces further confirms SAC structural instability and aggregation under reducing atmospheres in Fig. 6a (a key sintering trigger).[104] Using DFT calculations and P-T phase diagrams, researchers investigated stable Rh-modified CeO_2(111) structures, including RhO_x clusters (x = 1–3), supported Rh single atoms ($Rh_1/Ce_{48}O_{96}$), Rh clusters ($Rh_3/Ce_{48}O_{96}$), Rh-doped surfaces

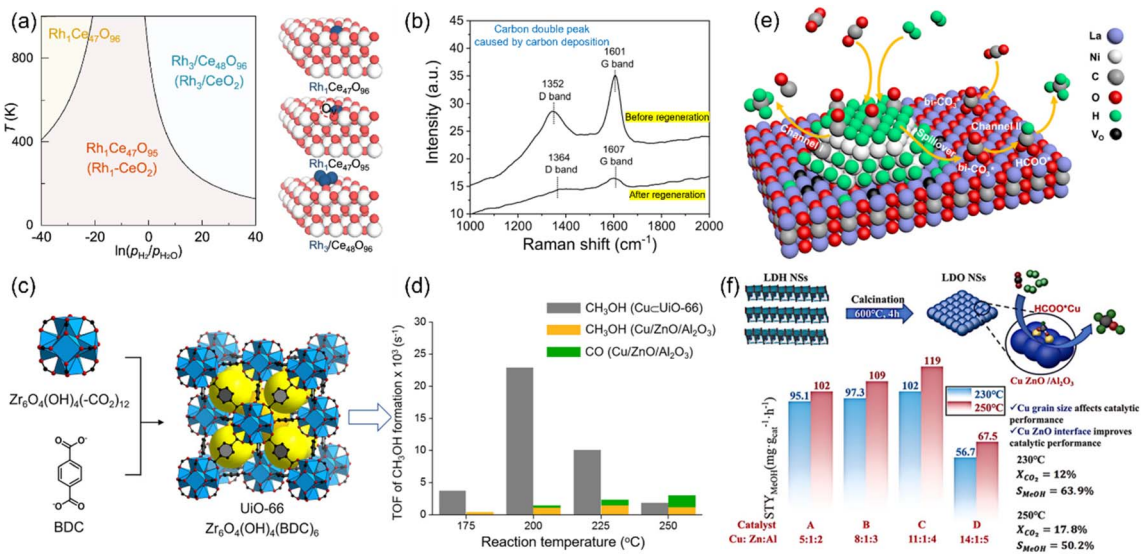

Fig. 6 Several principal physical and chemical processes driving SAC deactivation. (a) Stability and structural analysis of Rh-modified CeO_2(111) surfaces. (Left) Calculated phase diagrams under a reducing atmosphere; (right) optimized atomic structures of Rh-doped CeO_2(111) ($Rh_1Ce_{47}O_{96}$); reproduced with permission.[104] Copyright 2025, Springer Nature. (b) The Raman spectrum obtained after a 4-hour long-term stability test on activated $CuFeO_2$. The reaction was carried out under a pressure of 1 bar (with a hydrogen-to-carbon dioxide ratio of 3 : 1), with an air flow rate of 2400 millilitres per hour per gram of the catalyst, and a temperature of 320 °C; carbon deposition on activated $CuFeO_2$ before and after regeneration; reproduced with permission.[91] Copyright 2022, Springer Nature. (c) Encapsulating Cu nanoparticles/sites within Zr-MOF (UiO-66) frameworks and (d) its TOF of product formation as various reaction temperatures; reproduced with permission.[105] Copyright 2016, American Chemical Society. (e) Ni/La-doped CeO_2 catalysts with interfacial oxygen vacancies as catalysts for CO_2 hydrogenation; reproduced with permission.[106] Copyright 2024, American Chemical Society. (f) Schematic of the Cu–Zn–Al LDH-derived catalysts *via* physical confinement and interface engineering in CO_2 hydrogenation. The grey, blue, yellow, red, pink, and brown balls represent Ni, Cu, Mg, O, H, and C atoms, respectively; reproduced with permission.[107] Copyright 2025, American Chemical Society.

($Rh_1Ce_{47}O_{96}$), and Rh-doped surfaces with oxygen vacancies ($Rh_1Ce_{47}O_{95}$). The results show that Rh doping is thermodynamically preferred, with oxygen vacancies forming adjacent to Rh dopants under typical conditions; increasing the reducing atmosphere temperature and pressure stabilizes Rh clusters over single atoms, inducing sintering consistent with Ir aggregation in Ir_1–In_2O_3. The single-atom Rh-doped $CeO_2(111)$ (with O_v) and $CeO_2(111)$-supported Rh clusters were selected for further study, offering insights into SAC sintering-related structural evolution.

Strong metal–support interactions (SMSIs) are essential for optimizing the performance of supported metal catalysts by tuning the metal–oxide interface structures, yet excessive SMSI can paradoxically lead to encapsulation phenomena that reduce active site accessibility.[90] The balance between sufficient anchoring strength to prevent sintering and appropriate electronic modulation represents a critical design consideration.

3.3.2 Carbon deposition and surface reconstruction. In CO_2 hydrogenation reaction systems, existing studies generally posit that carbon deposition and surface restructuring constitute core mechanisms leading to SAC deactivation.[101,108,109] Accumulated carbon formed at metal–support interfaces or oxygen vacancy regions not only physically covers single-atom active sites but also causes local electronic structure changes, thereby disrupting reactant adsorption/desorption equilibrium and blocking key pathways required for ethanol production. Taking iron-based carbide systems as examples, calculations on various χ-Fe_5C_2 surfaces under different carbon coverage conditions reveal that as subsurface C occupancy increases, activation energies for direct CO dissociation significantly increase, markedly weakening the catalyst's CO activation rate.[110] The mechanistic basis lies in subsurface C extracting electrons from surface Fe atoms, resulting in decreased Fe atom charge density, thereby weakening their CO activation capability. This charge depletion effect reduces catalytically active sites at metal–carbon interfaces, causes local interface reconstruction, and ultimately leads to SAC deactivation under carbon-rich conditions.[111]

In experimental systems for CO_2 hydrogenation to long-chain olefins, long-term operation of iron-based carbide catalysts reveals surface carbon deposition leading to performance decline.[91] Experimental data indicate that after long-term stability tests, C_{2+} alkene selectivity significantly decreases. Meanwhile, carbon double peaks (disordered carbon D-band $\sim$1350 cm^{-1}; graphite G-band $\sim$1600 cm^{-1}) in Raman spectra confirm catalyst surface carbon deposition (Fig. 6b). Therefore, reduced C_{2+} product selectivity is intimately related to carbon deposition on catalyst active sites, as carbon deposits directly cover interface sites where CO insertion can occur, preventing catalysts from retaining C–C coupling pathways and ultimately resulting in significant reductions in C_{2+} product formation efficiency.

3.3.3 Stabilization strategies: physical confinement and chemical anchoring. The aforementioned deactivation pathways can be mitigated through physical confinement and chemical anchoring strategies. One widely validated approach involves confining single atoms within "restricted structures" constructed using MOFs or zeolites as precursors, which can inhibit single-atom migration and sintering at high temperatures and in reducing atmospheres, thereby significantly extending catalyst lifetimes. Recent research demonstrates that encapsulating Cu nanoparticles/sites within Zr-MOF (UiO-66) frameworks improves their thermal stability and selectivity, enabling SACs to retain high dispersion at elevated temperatures and reduce sintering rates (Fig. 6c and d).[105] This study fully demonstrates the unique advantages of rigid supports and restricted structures in maintaining SAC active site dispersion.

Another strategic approach involves enhancing single-atom active site stability through second metal or rare earth element doping.[112,113] Common methods include adding rare earth metals such as La and Ce to supports to form stronger metal–oxygen coordination and improved defect structures, thereby improving CO_2 hydrogenation activity.[114] Ni/La-doped CeO_2 catalysts demonstrate unprecedented catalytic performance in RWGS reactions (Fig. 6e), as La-doped oxides enhance interaction energies between metal sites and supports, significantly reducing metal atom migration energies and delaying high-temperature sintering/reconstruction processes.[106] Especially in CO_2 hydrogenation catalysis, modifying oxide supports with elements such as La and Ce significantly improves metal particle dispersion and thermal stability, substantially reducing activity loss rates under certain temperature and cycling conditions.

Recent advances in layered double hydroxides (LDHs) as supports for noble-metal SACs have demonstrated exceptional metal–support interactions that enhance both activity and stability.[115–117] LDHs offer distinct advantages including ordered and adjustable crystal structures, two-dimensional layered architectures possessing large specific surface areas, facile synthesis with cost-effectiveness, and strong co-catalytic metal–support interactions between LDHs and noble-metal single atoms.[118,119] Cui *et al.* developed Cu–Zn–Al LDH catalysts for CO_2-to-methanol conversion, achieving high stability and selectivity (Fig. 6f).[107] The LDH structure provides physical confinement and strong chemical anchoring, preventing Cu site aggregation and enhancing metal dispersion. These optimized metal–support interactions contribute to superior catalytic performance and durability, highlighting the effectiveness of stabilization strategies in CO_2 hydrogenation.

3.4 Advanced characterization and mechanistic understanding

Advanced characterization techniques such as *operando* X-ray methods, FTIR analysis, and DFT calculations have been utilized to elucidate catalytic mechanisms, revealing how structural properties and composition influence C–C coupling and optimize the conversion of CO_2 to ethanol.[117] X-ray absorption spectroscopy (XAS) combined with extended X-ray absorption fine structure (EXAFS) provides atomic-level structural information regarding coordination numbers, bond distances, and local geometric arrangements around single-atom centres (Fig. 7a).[120–122]

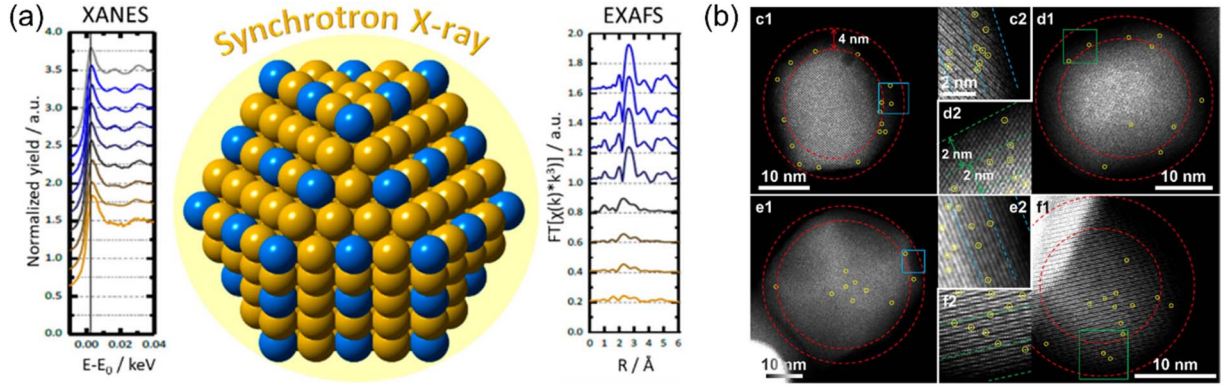

Fig. 7 Advanced characterization techniques in the study of CO_2 hydrogenation reactions over SACs. (a) XAS combined with EXAFS characterization on SACs; reproduced with permission.[120] Copyright 2024, American Chemical Society. (b) HAADF-STEM for visualization of SACs; reproduced with permission.[122] Copyright 2025, American Chemical Society.

Although existing conventional characterization techniques have strong capabilities in detecting reaction intermediates and local coordination environments, they also have certain inherent limitations. In particular, their time resolution is often insufficient to directly capture ultrafast transient species and short-lived intermediates, which often play a crucial role in the C–C coupling step for preparing ethanol.[103] At the same time, the spectral signal overlap and average measurement of some characterization techniques can also mask the identification of low-concentration or dynamically changing active species under actual reaction conditions.[123] Therefore, the direct observation of the key steps in CO_2 hydrogenation for ethanol production remains challenging. Usually, this requires methods with higher time resolution for auxiliary research, such as time-resolved spectroscopy and advanced computational simulations, to achieve a more comprehensive understanding of the mechanism.

High-angle annular dark-field scanning transmission electron microscopy (HAADF-STEM) enables direct visualization of atomically dispersed metal centres, confirming single-atom dispersion and detecting incipient aggregation phenomena (Fig. 7b).[124,125] *In situ* DRIFTS reveals real-time intermediate evolution during catalytic processes, identifying key surface species and their transformation pathways under working conditions.[21,126,127] The significance of particle sizes in determining catalytic properties is well-established, with the transition of metal active sites from nanoparticles to sub-nanometre clusters and then to single atoms introducing differences in metal atom aggregation and coordination structures in supported catalysts.[128,129] These structural variations profoundly impact electronic properties, intermediate binding energies, and ultimately catalytic performance.[130] DFT calculations complement experimental investigations by providing atomistic insights into electronic structures, reaction pathways, and energy landscapes. Microkinetic modelling based on DFT-derived activation barriers enables quantitative prediction of product selectivities and identification of rate-determining steps.[131,132] Computational studies using density functional calculations and microkinetic simulations have found that introducing metal single atoms in In_2O_3 can significantly change the reaction pathway and the stability of intermediates, providing valuable guidance for future catalyst screening and optimization.[76]

3.5 Emerging frontiers: machine learning and high-throughput screening

Machine learning is emerging as a powerful tool for predicting SAC stability and optimizing reaction pathways, opening new avenues for accelerated catalyst discovery and rational design (Fig. 8).[128,133,134] Machine learning algorithms trained on large databases of computational and experimental data can identify complex structure–activity relationships that would be challenging to discern through traditional approaches.[135] These models can predict optimal coordination environments, metal–support combinations, and operating conditions for target selectivities, dramatically reducing the experimental search space.[134,136] High-throughput computational screening combined with machine learning enables systematic

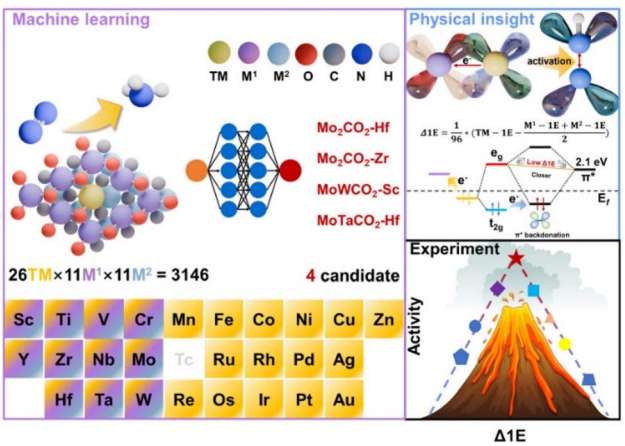

Fig. 8 Machine learning accelerated screening advanced single-atom anchored Mxene electrocatalyst; reproduced with permission.[134] Copyright 2025, American Chemical Society.

exploration of vast catalyst composition spaces, identifying promising candidates for subsequent experimental validation.[137,138] This integrated computational–experimental approach accelerates the catalyst discovery cycle, enabling rapid translation of fundamental mechanistic insights into practical catalytic systems.

SACs can significantly reduce reaction energy barriers and enhance product selectivity in complex C–C coupling reactions such as CO_2 hydrogenation to ethanol.[21,23] However, to ensure long-term stable operation of SACs in industrial applications, it is essential not only to comprehensively understand SAC failure environments and mechanisms but also to optimize material design through single-atom anchoring and interface engineering strategies, thereby achieving large-scale commercial application of SAC technologies.[117,139] Recent advances in single-atom heterogeneous catalysts demonstrate promising opportunities in CO_2 hydrogenation, with atomically dispersed metals on supports showing superior performance compared to traditional nanoparticulate catalysts.[26,44,76,125,140]

4. Emerging strategies and future directions

The translation of SAC breakthroughs from laboratory demonstrations to industrial-scale CO_2-to-ethanol conversion necessitates addressing critical challenges in synthesis scalability, renewable energy integration, and process engineering.[141] This section examines three interconnected frontiers that will determine the commercial viability of SAC technologies: (1) advanced synthesis techniques enabling precise atomic-level control while maintaining manufacturability, (2) strategic coupling with renewable H_2 production infrastructure, and (3) industrial scalability through optimized reactor design and process intensification. Collectively, these emerging strategies provide a roadmap for transitioning SAC-catalysed CO_2 hydrogenation from proof-of-concept studies to practical carbon utilization technologies.

4.1 Advanced synthesis techniques for precise atomic-level control

Beyond monometallic single-atom and sub-nanocluster architectures, ALD also enables the precise fabrication of well-defined bimetallic dimeric structures: Zhang *et al.* successfully synthesized high-quality Pt–Ru bimetallic dimers with a one-to-one bonding configuration *via* a tailored ALD process, which delivered over 50 times higher HER activity alongside excellent stability relative to commercial Pt/C catalysts, as verified by X-ray absorption spectroscopy characterization. Meanwhile, related *in situ* characterization studies (HAADF-STEM and XANES/EXAFS) further confirmed that the single-atom/sub-nanocluster catalysts prepared by ALD could achieve a large number of single-atom sites in a low coordination state, fully demonstrating the unique advantages of ALD in achieving high-quality single-atom dispersion, constructing well-defined bimetallic nanostructures, and regulating electronic and coordination environments. The precise construction of SAC active sites at the atomic scale and their dynamic restructuring under operating conditions constitute the pivotal challenge in advancing SACs from laboratory curiosities to industrial workhorses.[29] Atomic layer deposition (ALD) has gained increasing attention as a technique for deposition of noble metals and metal oxides due to its ability to prepare uniform and conformal thin films, as well as to deposit of uniformly distributed particles ranging from single atoms to sub-nanometre clusters to nanoparticles in high-aspect-ratio structures and porous materials.[142–144] ALD can achieve precise deposition of precursors at the nanometre and even atomic scales due to its "self-limiting" layer-by-layer growth mechanism, as illustrated in Fig. 9a.[143] Additionally, this technology can precisely construct metal active sites spanning the entire spectrum from discrete single atoms through sub-nanometre clusters to nanoparticles on the same platform by regulating the number of deposition cycles.[145,146]

SACs prepared by ALD have demonstrated remarkable performances in selective hydrogenation reactions.[145] Taking the Pt single-atom/sub-nanocluster catalyst prepared by ALD on graphene as an exemplary system, compared with traditional Pt/C catalysts, this single-atom catalyst exhibits significantly enhanced structural uniformity and up to 10-fold improvement in catalytic activity. Beyond monometallic single-atom and sub-nanocluster architectures, ALD also enables the precise fabrication of well-defined bimetallic dimeric structures: Zhang *et al.* successfully synthesized high-quality Pt–Ru bimetallic dimers with a one-to-one bonding configuration *via* a tailored ALD process, which delivered over 50 times higher HER activity alongside excellent stability relative to commercial Pt/C catalysts, as verified by X-ray absorption spectroscopy characterization (Fig. 9b).[147] Meanwhile, related *in situ* characterization studies (HAADF-STEM and XANES/EXAFS) further confirmed that the single-atom/sub-nanocluster catalysts prepared by ALD could achieve a large number of single-atom sites in a low coordination state, fully demonstrating the unique advantages of ALD in achieving high-quality single-atom dispersion and regulating electronic and coordination environments.[147,148]

Therefore, ALD not only enables "production of single atoms" but also allows for precise control over site density and spatial distribution.[143] This technology can precisely regulate metal loading to the wt% or even ppm level by adjusting ALD cycle numbers, precursor dosage, and substrate surface functional group density and controlling the selective growth of isolated atoms and clusters, thereby preparing SACs with exceptional performance.

Contemporary ALD methodologies have evolved into various sophisticated variants to meet the preparation requirements for high-performance SACs. Diluted ALD (DALD), systematically reduces metal loading from traditional ALD high-load regimes (1 atom per nm^2) to ultra-low levels of 0.01–0.04 atoms per nm^2 within a single DALD cycle by adjusting the precursor molar fraction, achieving precise sub-monolayer control of metal deposition amount. This method not only minimizes precious metal usage at the atomic scale but also maintains the unique catalytic activity and selectivity of SACs through formation of

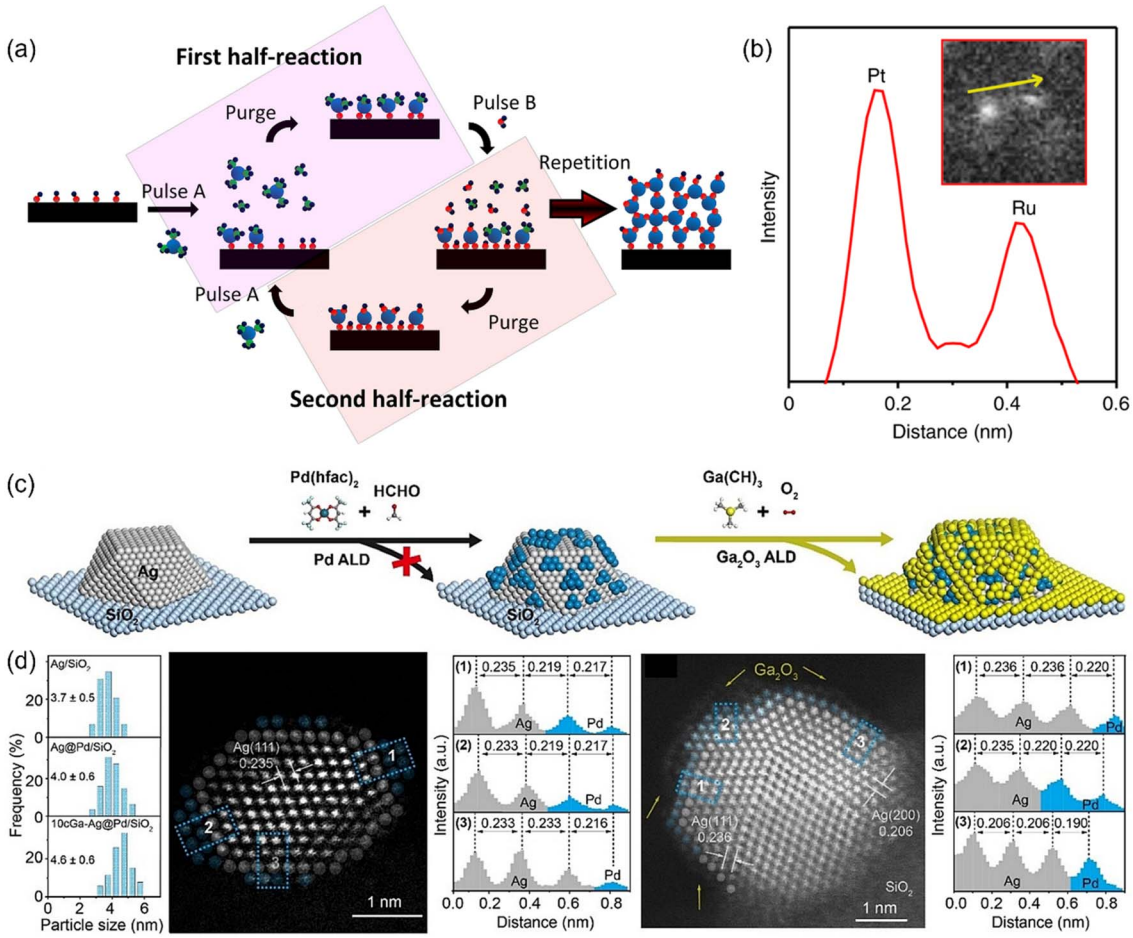

Fig. 9 ALD and diluted ALD mechanisms for SAC synthesis. (a) Schematic representation of the ALD technique using a binary (AB) precursor system; reproduced with permission.[143] Copyright 2021, American Chemical Society. (b) Pt–Ru dual-metal dimers synthesized by ALD; reproduced with permission.[147] Copyright 2019, Springer Nature. (c and d) Synthesis, particle size distribution and atomic-resolution HAADF-STEM characterization of the Ga_2O_3-coated Ag@Pd/SiO_2 core–shell bimetallic catalyst; reproduced with permission.[152] Copyright 2021, John Wiley and Sons.

strong metal–support interactions, providing inspiration for industrial application of single-atom catalysts.[100]

However, the practical application of the synthesis strategy based on ALD for the production of industrial-scale catalysts still faces significant challenges. The inherently slow cycling characteristics of ALD significantly limit the production volume and efficiency, while the demand for special precursors, controlled environments, and complex instruments further increases the production cost.[149] Therefore, although ALD can achieve precise atomic control of SACs on a laboratory scale, its direct application in the sensitive industrial sectors is still limited. Future research should focus on converting ALD and other atomic-level control technologies into more scalable and economically feasible synthesis routes.

Meanwhile, the precise construction of SACs at the atomic scale does not inherently guarantee excellent catalytic performance. The "working state" structure generated by dynamic restructuring under operating conditions represents the active centre that directly participates in and determines catalytic performance. Recent years have witnessed extensive *operando* characterization studies of SACs revealing that many single-atomic sites undergo reversible or irreversible reconstructions under electrochemical or gas-phase high-temperature reaction conditions.[150] This manifests primarily as dynamic aggregation of single atoms into dimers or sub-nanoclusters under reaction conditions, as well as formation of coordination complexes with reactants (such as CO, CO_2, and carbonyl compounds), thereby inducing local geometric and valence state changes that significantly affect catalytic performance.

Comprehensive *operando* spectroscopy in an electrochemical CO_2 reduction system revealed that N–Cu coordinated single-atomic sites undergo local Cu–N bond breaking to form "low-coordinated dynamic active configurations" under working potentials. This configuration causes CO selectivity to increase sharply within the potential range of −0.7 V to −0.8 V (faradaic efficiency-CO increases to 65–70%), exhibiting higher activity than static coordination structures. This comprehensively reveals the phenomenon that single-atomic sites can "spontaneously reconfigure into low-coordinated forms or aggregates" under real reaction conditions, establishing that SAC synthesis

strategies must account for dynamic restructuring under working conditions.

Recent advances have demonstrated that manufacturing single-atom alloys (SAAs) through an "islanding effect" strategy achieves 100% CO selectivity and over 55 times higher reverse water–gas shift rate than alloys with cluster sites, with SAA catalysts exhibiting 3–4 times higher RWGS rates than SAAs synthesized *via* dilution methods (Fig. 9c).[151] Based on the above research progress, we recognize that ALD, as a mature technology for achieving precise single-atom loading at the atomic scale, can produce SACs with high uniformity and low loading of highly active sites. However, to successfully apply ALD-synthesized SACs to CO_2 hydrogenation reactions, combining ALD synthesis with consideration of dynamic restructuring during reaction processes constitutes the key approach for forming highly selective and durable $CO_2 \rightarrow C_2$ catalytic systems. Therefore, utilizing ALD technology to manufacture "controllably and reversibly restructured" SAC sites represents a critical research direction for improving catalytic efficiency and lifetime.

4.2 Integration with renewable H_2 production infrastructure

To achieve industrialization of CO_2 hydrogenation, access to reliable and sustainable H_2 sources constitutes a fundamental prerequisite (Fig. 10a).[153] Proton exchange membrane water electrolyzers (PEMWEs) exhibit significant advantages including high H_2 production purity, rapid response speed, and capability to directly produce H_2 under elevated pressure to reduce downstream compression requirements.[2,154] PEM electrolyzers have higher power densities, output H_2 pressures and faster response times than alkaline systems, generally making them better suited to coupling with renewable energy sources directly.[155,156] These features position PEMWEs as the preferred solution for on-demand H_2 supply. Therefore, coupled systems consisting of PEM electrolyzers and downstream CO_2 hydrogenation reactors (driving SACs) are regarded as effective pathways to achieve industrialization.[157]

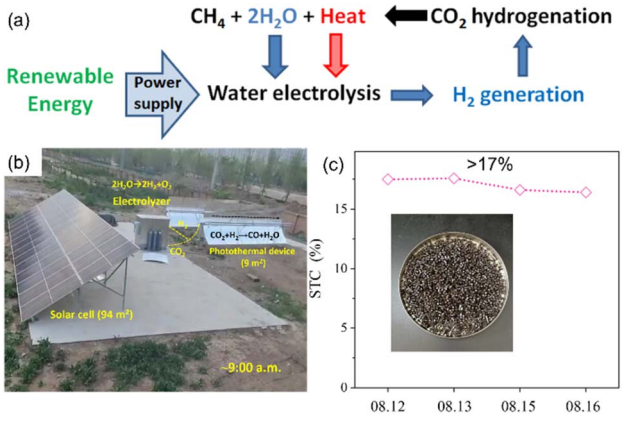

Fig. 10 Renewable H_2 production systems coupled with CO_2 hydrogenation configurations. (a) Schematic of renewable energy-driven water electrolysis for H_2 production and subsequent CO_2 hydrogenation; reproduced with permission.[153] Copyright 2019, Springer Nature. (b) Outdoor performance of the PV-EC water splitting system for H_2 supply in CO_2 hydrogenation; (c) solar-to-chemical conversion (STC) efficiency of the integrated system under ambient sunlight irradiation (inset: a photograph of the granulated 2D $Ni_1Ag_{0.02}O_1$ catalyst); reproduced with permission.[10] Copyright 2024, The American Association for the Advancement of Science.

Current studies have reported that under a gas hourly space velocity (GHSV) of 4255 h^{-1} and at 150 °C, Ru–N–C single-atom catalysts achieved 99% CO conversion rate and 95% CH_4 selectivity, demonstrating excellent catalytic activity and stability.[127] Combining the characteristic that PEMWEs can respond to power changes within seconds, it becomes theoretically possible to construct a truly "on-demand H_2 supply with dynamic selectivity regulation" reaction coupling system. However, "PEMWE-SAC coupling" transcends mere device integration, involving cross-scale interface dynamics regulation. H_2 supply modes under real conditions (batch/load fluctuations), gas purity, and transient potential distribution at electrochemical interfaces all profoundly affect the electronic state, coordination environment, and stability of SACs. Therefore, PEMWE output behaviour should be regarded as the "upstream boundary condition" of the SAC catalyst electronic structure, rather than merely a H_2 supply component.

Recent breakthrough research provides compelling evidence for this paradigm. By constructing an alloyed Pt-SAC and directly applying it to PEM water electrolyzers for real-condition testing, stable operation for 1000 hours at 1 A cm^{-2} and 80 °C was achieved, with voltage increasing only from 1.820 V to 1.881 V, corresponding to an average attenuation rate of merely 0.061 mV h^{-1}.[158] Meanwhile, after 20 000 cyclic voltammetry (CV) cycles, the electrochemical activity of the alloyed Pt-SAC exhibited no attenuation, demonstrating exceptional anti-reconfiguration capability under dynamic potential perturbations. These data compellingly demonstrate that when SACs are deeply coupled with PEMWEs, their structural stability is not solely determined by material properties but is also regulated by the dynamic electrochemical environment of the upstream electrolyzer.

Another landmark breakthrough in large-scale coupled systems further corroborates the feasibility of integrating renewable H_2 production with CO_2 hydrogenation *via* SACs. Notably, scalable artificial photosynthesis systems composed of PV electrolysis and photothermal CO_2 hydrogenation are traditionally limited by inefficient photothermal CO_2 hydrogenation under weak sunlight irradiation (Fig. 10b and c). To address this, Li *et al.* reported the synthesis of Ag single-atom-supported NiO nanosheets (2D $Ni_1Ag_{0.02}O_1$) for photothermal CO_2 hydrogenation, which achieved a CO production rate of 1065 mmol g^{-1} h^{-1} under 1-sun irradiation. This excellent performance was attributed to the coupling effect of Ag–O–Ni sites, which enhanced CO_2 hydrogenation and weakened CO adsorption, leading to a CO yield of 1434 mmol g^{-1} h^{-1} at 300 °C. Furthermore, they integrated the 2D $Ni_1Ag_{0.02}O_1$-catalyzed photothermal reverse water–gas shift reaction with commercial PV electrolytic water splitting to construct a 103-m^2 scale artificial photosynthesis system ($CO_2 + H_2O \rightarrow CO + H_2 + O_2$), which achieved a green syngas output of more than 22 m^3 per

day with an adjustable H_2/CO ratio (0.4–3) and a photochemical energy conversion efficiency exceeding 17% (Fig. 10b and c).[10]

From the reaction kinetics perspective of SACs, coupling PEMWEs with high-purity H_2 helps stabilize key hydrogenation intermediates, thereby strengthening the C–C coupling pathway. For example, Ir_1–In_2O_3 exhibits ethanol selectivity exceeding 99% under 60 bar and 473 K conditions. Its high reactivity has been unambiguously demonstrated to depend on bifunctional sites: CO_2 is activated on In_2O_3–O_v, while H_2 is activated at Ir single-atom sites. In such systems, using high-purity H_2 provided by a PEMWE without CO, CH_4, *etc.*, can effectively avoid poisoning and deactivation of active metal sites due to impurity adsorption, thus ensuring continuous expression of efficient H_2 activation capability.[159,160] This further indicates that coupling of PEMWEs and SACs can not only improve carbon–hydrogen activation efficiency but also achieve complementary and synergistic "clean hydrogen-precise activation" between energy input and interface reactions.

PEM water electrolysis technology is gaining prominence in the quest for sustainable H_2 production due to its efficiency (60–90%), scalability, and versatility, with capability to quickly respond to power variations and therefore enabling integration with renewable power sources such as solar and wind, whose output can change significantly. The coupling of single-atom catalysts with PEM electrolysis for on-demand integration represents a low-carbon pathway with industrial significance. However, to achieve coexistence of high selectivity, continuity, and economic viability, this coupled system still requires simultaneous research and design in two aspects: "dynamic operation strategy of the electrolyzer" and "catalyst adaptability to transient hydrogenation conditions".[161–163]

4.3 Industrial scalability through process intensification and reactor engineering

SACs demonstrate remarkable industrial scalability potential in CO_2 hydrogenation to ethanol processes. Compared with traditional Cu–Fe catalytic systems, SACs exhibit unique competitiveness in aspects including C–C coupling pathway regulation, ethanol selectivity enhancement, reaction energy consumption reduction, and maximization of single-metal utilization.[76] Based on the HAADF-STEM study of single-atom Co/MoS_2 by Ding *et al.*,[164] we found that SACs achieved metal atom utilization approaching the theoretical maximum by dispersing metal atoms as isolated sites onto supports. This results in precious metal requirements per unit product that are one order of magnitude lower compared to traditional nano/cluster catalysts, significantly reducing catalyst preparation costs from the source.

Simultaneously, the capability of SACs to regulate C–C coupling energy barriers means that equivalent or even higher ethanol yields can be achieved at lower temperatures and pressures, significantly reducing reaction system energy consumption and carbon emissions. For instance, Ir_1–In_2O_3 achieves >99% ethanol selectivity at 473 K and 60 bar, while traditional Cu–Fe catalysts typically require higher temperatures and pressures, with product selectivity and stability exhibiting substantial fluctuations. In contrast, SACs demonstrate potential for high selectivity under milder conditions.[76] More importantly, with gradual maturation of large-scale preparation routes such as ALD and vapor-phase precursor atomization, SACs have achieved stable batch production output of 1 kg per day, laying a solid preparation process foundation for industrial application.

For industrialization of CO_2 hydrogenation to ethanol production, pilot-scale reactor designs are equally crucial. CO_2 hydrogenation to ethanol is a thermochemical reaction requiring precise temperature control and C–C coupling promotion. Even if SACs exhibit exceptional performance, if reactors cannot effectively manage heat release, SAC advantages will be difficult to scale up to industrial levels. Therefore, pilot tests and industrial demonstration projects often adopt engineering design methods such as multi-stage adiabatic fixed

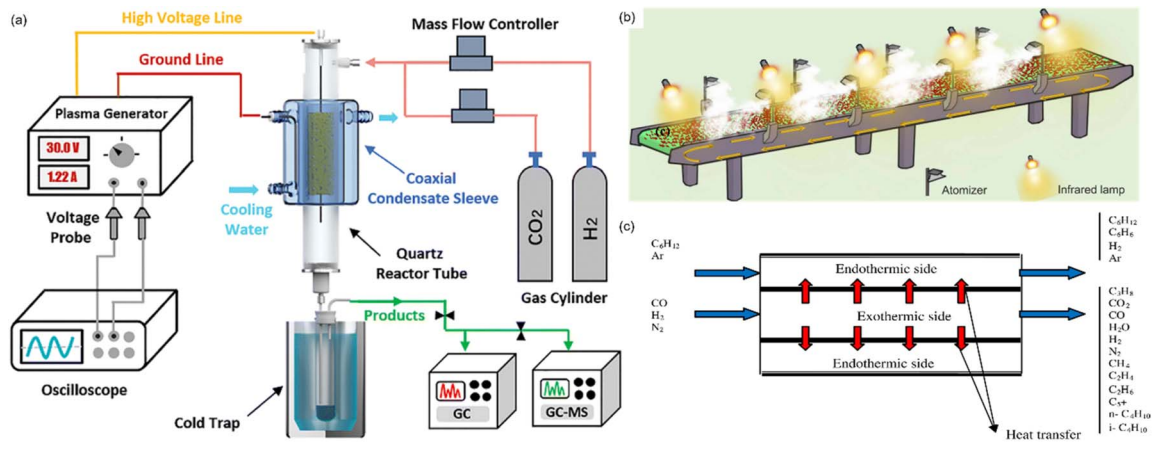

Fig. 11 Industrial scalability through process intensification and reactor engineering and for the CO_2 hydrogenation to ethanol system. (a) A non-thermal plasma catalyst coupled catalytic system with feed gas, analysis and a power supply module reactor for CO_2 hydrogenation to ethanol; reproduced with permission.[165] Copyright 2013, Royal Society of Chemistry. (b) The scheme for the production line that is based on the precursor-atomization strategy; reproduced with permission.[166] Copyright 2022, Springer Nature. (c) A schematic of the co-current recuperative coupled reactor; reproduced with permission.[167] Copyright 2010, Elsevier.

beds connected in series to control the extent of reactor heat release and maintain optimal reaction temperature gradients. Complementing the mild-condition advantages of SACs, non-thermal plasma-assisted catalysis is another promising approach for efficient CO_2 hydrogenation to ethanol under ambient conditions, supported by the reactor design illustrated in Fig. 11a.[165] Traditional processes require temperatures above 300 °C to activate CO_2, which is unfavourable for ethanol formation, so researchers used non-thermal plasma for ambient CO_2 activation and a Cu(I)-MOF catalyst (Cu(I)-HKUST-17.5), achieving 41.2% CO_2 conversion and 62.9% ethanol selectivity. Control experiments confirmed that Cu(I) sites are critical for C–C coupling, and a new synergistic mechanism between non-thermal plasma and the catalyst's Cu(I)/Cu(II) sites was proposed *via* DRIFTS analysis, verifying industrial feasibility of this mild route. More importantly, with gradual maturation of large-scale preparation routes such as ALD and vapor-phase precursor atomization, SACs have achieved stable batch production output of 1 kg per day, laying a solid preparation process foundation for industrial application.

As previously stated, thermal coupling of water electrolyzers and CO_2 hydrogenation systems offers opportunities to increase exergy efficiency, where thermal energy required to split water into H_2 and O_2 during electrolysis can be compensated by heat generated during CO_2 hydrogenation reactions. This integrated approach not only improves overall system efficiency but also addresses the highly exothermic nature of the Sabatier reaction, which generates substantial heat that must be removed to maintain relatively low temperatures and prevent catalyst sintering. Therefore, industrial pilot tests should prioritize integrating large-scale, low-cost SAC production routes (Fig. 11b) with heat transfer-enhanced modular reactor designs (Fig. 11c).[166,167] This integration aims to convert high laboratory-scale selectivity into stable production capacity for continuous manufacturing, ultimately achieving an optimal balance among economic feasibility, system lifetime, and safety. The significance of integrated systems extends beyond individual component optimization to encompass cascaded electrochemical and biochemical processes that utilize ambient conditions while achieving enhanced productivity of multi-carbon chemicals, representing a paradigm shift toward holistic process design for CO_2 utilization technologies.

5. Conclusion and outlook

This comprehensive review has examined the atomic-level engineering principles governing single-atom catalyst design for selective CO_2 hydrogenation to ethanol, establishing fundamental structure–activity relationships that bridge the gap between mechanistic understanding and practical catalyst development (Fig. 12). Single-atom catalysts have emerged as transformative platforms for addressing the intrinsic challenges of C–C bond formation in CO_2 conversion, enabling unprecedented control over reaction selectivity through precise modulation of electronic structures and coordination environments at the atomic scale.

The mechanistic analyses presented herein establish that selective ethanol formation fundamentally requires overcoming competing thermodynamic and kinetic pathways that favour C_1 products. The ternary interfacial architecture comprising "isolated metal-defect site-carrier cation" assemblies represents the minimal functional unit capable of biasing reaction pathways toward C_2 products, as exemplified by breakthrough systems such as Ir_1–P_x/In_2O_3 achieving >99% ethanol selectivity with

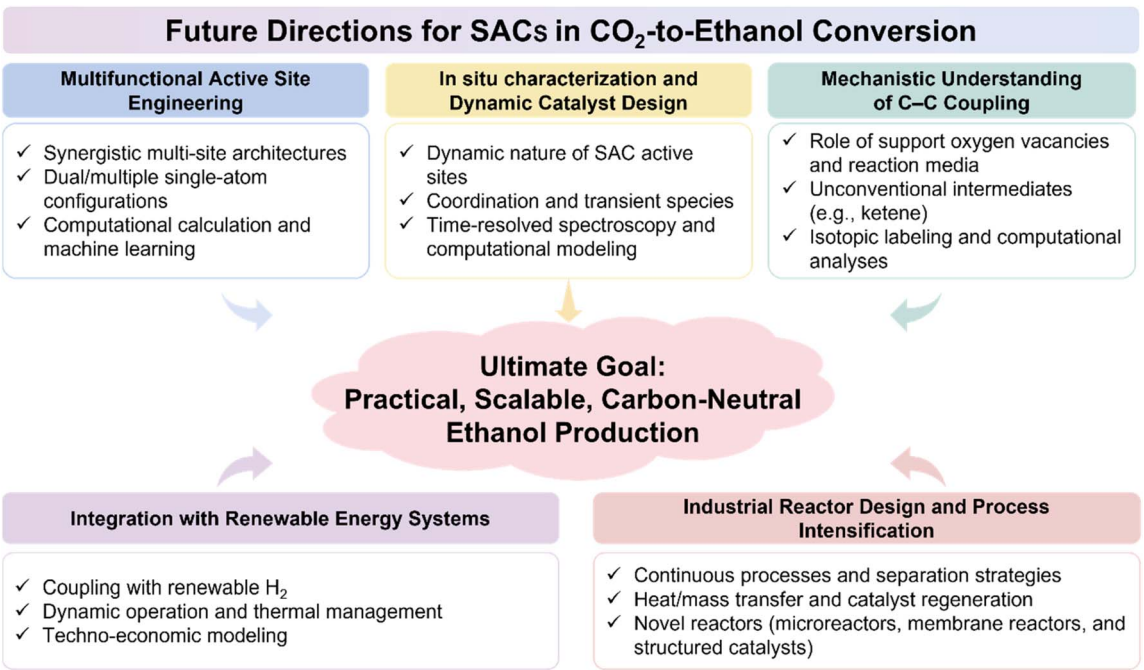

Fig. 12 Schematic illustration of future directions for development of CO_2 hydrogenation to ethanol over SACs.

turnover frequencies exceeding 2000 h^{-1} under industrially relevant conditions. The atomic-level design of catalysts through systematic examination of CO_2 hydrogenation reaction pathways has provided valuable insights into rational catalyst engineering. These achievements validate the paradigm that electronic structure engineering at single-atom active sites can achieve "reaction path selectivity reconstruction", rendering C–C coupling kinetically superior to methanation and over–hydrogenation pathways.

Despite remarkable progress in laboratory-scale demonstrations, several critical challenges must be addressed to enable industrial deployment of SAC-catalysed CO_2-to-ethanol conversion technologies. First, catalyst stability under realistic operating conditions remains a primary bottleneck. While advanced characterization techniques have elucidated deactivation mechanisms including site sintering, carbon deposition, and support interactions, translating these mechanistic insights into robust stabilization strategies requires further investigation. Recent advances in synthesis strategies for SACs have highlighted the importance of understanding dynamic restructuring phenomena under working conditions, suggesting that "controllably reversible" active site configurations may represent an optimal design target rather than static structural stability.

Second, the scalability of SAC synthesis methodologies demands continued innovation. While atomic layer deposition and related techniques have demonstrated precise control over single-atom dispersion, achieving economically viable production scales (multi-kilogram quantities) with maintained atomic uniformity presents formidable engineering challenges. The issue of product selectivity in CO_2 hydrogenation emphasizes the need for synthesis strategies that can be translated from laboratory to industrial scales while preserving the unique electronic and geometric properties of single-atom sites. Future research should prioritize development of continuous synthesis processes and quality control methodologies suitable for industrial implementation.

Looking forward, several promising research directions warrant intensive investigation:

(1) Multifunctional active site engineering: the next generation of SAC systems should incorporate synergistic multi-site architectures that decouple individual reaction steps (CO_2 activation, H_2 dissociation, and C–C coupling) onto distinct but cooperative active centres. Dual or multiple single-atom configurations, potentially combining different transition metals with tailored coordination environments, may enable simultaneous optimization of conflicting catalytic requirements. Computational screening guided by machine learning algorithms can accelerate identification of optimal metal combinations and support materials, dramatically expanding the accessible design space beyond empirical exploration.

(2) *Operando* understanding and dynamic catalyst design: future studies must embrace the dynamic nature of SAC active sites under working conditions. Rather than viewing structural evolution as undesired deactivation, researchers should explore how reversible coordination changes, transient intermediate species, and adaptive surface configurations can be harnessed to enhance catalytic performance. Advanced time-resolved spectroscopic and microscopic techniques coupled with computational modelling will be essential for capturing these dynamic phenomena and translating them into rational design principles.

(3) Integration with renewable energy systems: the coupling of SAC-catalysed CO_2 hydrogenation with renewable H_2 production infrastructure represents a critical pathway toward carbon-neutral fuel synthesis. Beyond technical integration, future research should address system-level optimization including dynamic operation strategies that accommodate renewable energy intermittency, thermal management across coupled electrochemical–thermochemical processes, and techno-economic modelling that quantifies pathway viability under realistic market conditions. The rapid response characteristics of PEM electrolyzers aligned with the exceptional selectivity of SACs under mild conditions suggest synergistic opportunities that remain largely unexplored.

(4) Mechanistic understanding of C–C coupling: despite significant progress, fundamental aspects of C–C bond formation mechanisms require deeper investigation. The precise role of support oxygen vacancies, the influence of reaction media (gas-phase *versus* liquid-phase conditions), and the potential involvement of unconventional intermediates (such as ketene or surface-bound acyl species) deserve systematic study. Isotopic labelling experiments combined with computational mechanistic analyses can resolve ambiguities regarding coupling pathways and identify rate-determining steps that represent the most promising targets for catalyst optimization.

(5) Industrial reactor design and process intensification: transitioning from batch laboratory reactors to continuous industrial processes necessitates addressing heat and mass transfer limitations, product separation strategies, and long-term catalyst regeneration protocols. Novel reactor configurations including microreactors, membrane reactors, and structured catalysts may offer advantages in thermal management and selectivity control. Process intensification strategies that integrate reaction and separation functions could dramatically improve overall system efficiency and economic viability.

In conclusion, single-atom catalysts have fundamentally transformed the landscape of selective CO_2 hydrogenation, demonstrating that atomic-level precision in catalyst design can overcome long-standing selectivity challenges. The convergence of advanced synthesis methodologies, sophisticated characterization techniques, computational modelling, and system engineering approaches positions the field at the threshold of practical carbon utilization technologies. Realizing the full potential of SAC-catalysed CO_2-to-ethanol conversion will require sustained interdisciplinary collaboration, spanning fundamental catalysis science, materials engineering, renewable energy integration, and process design. As the global imperative for carbon neutrality intensifies, the insights and strategies outlined in this review provide a comprehensive framework for advancing CO_2 utilization from laboratory demonstrations to industrial-scale implementation, contributing meaningfully to the ongoing transition toward sustainable energy systems.

Author contributions

All authors approved the final version of the manuscript. Wenyu Zheng, Yiming Liu, and Xiaohai Zhang: investigation, supervision, conceptualization, writing – original draft, writing review & editing. Shengjie Bai: visualization, investigation, conceptualization, supervision, writing – original draft, writing – review & editing. Aobing Li: visualization, writing – original draft, writing review & editing. Kelun Jiang and Feng Wang: writing review & editing. Ya liu, Yubin Chen, and Shaohua Shen: conceptualization, supervision.

Conflicts of interest

There are no conflicts to declare.

Data availability

No primary research results, software or code have been included and no new data were generated or analysed as part of this review.

Acknowledgements

This work was supported by the National Key R&D Program of China (2024YFF0506100), National Natural Science Foundation of China (No. 52406271), China Postdoctoral Science Foundation (No. 2024M762593 and GZC20241350), and Natural Science Foundation of Sichuan Province (No. 2026NSFSC1218). This work was supported by the HPC Platform, Xi'an Jiaotong University and Computing Center in Xi'an.

References

1 J. Ye, N. Dimitratos, L. M. Rossi, N. Thonemann, A. M. Beale and R. Wojcieszak, *Science*, 2025, **387**, eadn9388.
2 W. Fang, W. Guo, R. Lu, Y. Yan, X. Liu, D. Wu, F. M. Li, Y. Zhou, C. He, C. Xia, H. Niu, S. Wang, Y. Liu, Y. Mao, C. Zhang, B. You, Y. Pang, L. Duan, X. Yang, F. Song, T. Zhai, G. Wang, X. Guo, B. Tan, T. Yao, Z. Wang and B. Y. Xia, *Nature*, 2024, **626**, 86–91.
3 M. Liu, Y. Xu, Y. Meng, L. Wang, H. Wang, Y. Huang, N. Onishi, L. Wang, Z. Fan and Y. Himeda, *Adv. Energy Mater.*, 2022, **12**, 2200817.
4 J. Artz, T. E. Muller, K. Thenert, J. Kleinekorte, R. Meys, A. Sternberg, A. Bardow and W. Leitner, *Chem. Rev.*, 2018, **118**, 434–504.
5 S. Kar, D. Kim, A. Bin Mohamad Annuar, B. B. Sarma, M. Stanton, E. Lam, S. Bhattacharjee, S. Karak, H. F. Greer and E. Reisner, *Nat. Energy*, 2025, **10**, 448–459.
6 J. Liu, P. Li, S. Jia, Y. Wang, L. Jing, Z. Liu, J. Zhang, Q. Qian, X. Kang, X. Sun, Q. Zhu and B. Han, *Nat. Synth.*, 2025, **4**, 730–743.
7 Z. T. Sun, J. L. Huang, Z. J. Ji, K. X. Feng, D. Y. Liu, C. C. Wu and Y. Zhang, *ACS Catal.*, 2026, **16**, 3926–3941.
8 W. Liu, H. Zhao, X. Wu, J. Wu, L. Chou, G. Dury, W. Hu, M. V. Polynski, A. Subramanian, S. M. Kozlov and W. Liu, *ACS Catal.*, 2026, **16**, 3464–3478.
9 M. Zhang, L. Jia, M. Li, H. Peng, Y. Tan, S. Arvelli, Y. Huang, A. C. Neves, E. J. Oh and J. Zhao, *ACS Sustainable Chem. Eng.*, 2025, **13**, 5201–5209.
10 Y. Li, F. Meng, Q. Wu, D. Yuan, H. Wang, B. Liu, J. Wang, X. San, L. Gu and Q. Meng, *Sci. Adv.*, 2024, **10**, eadn5098.
11 Y. Wang, F. Xue, W. Zhang, D. Cao, M. Zhang, Z. Li, C. Zhan, Q. Kuang and Z. Xie, *Angew. Chem., Int. Ed.*, 2026, **65**, e21576.
12 S. Poto, D. Vico van Berkel, F. Gallucci and M. Fernanda Neira d'Angelo, *Chem. Eng. J.*, 2022, **435**, 134946.
13 F. W. Zhao, T. Zeng, X. L. Yang, Q. Wang, Y. Zhao, J. Zhou, X. F. Yang, C. F. Lin, H. X. Ben, N. X. Zhai, X. H. Yu, Y. Z. Yuan, X. K. Gu, X. Y. Li, Y. Q. Huang and X. S. Zhao, *ACS Catal.*, 2026, **16**, 2687–2697.
14 X. Wu, Y. Liu, J. Cheng, J. Zhang, Z. Mao, R. Zhang, B. Wang, S. Cui, H. Wang, J. Du, Z. Li and C. Li, *Angew. Chem., Int. Ed.*, 2026, **65**, e25886.
15 L. He, Y. Wang, C. Wang, Y. Zheng, A. Zhang, H. Wang and K. Li, *ACS Catal.*, 2026, **16**, 3216–3230.
16 H. Guzman, F. Salomone, S. Bensaid, M. Castellino, N. Russo and S. Hernandez, *ACS Appl. Mater. Interfaces*, 2022, **14**, 517–530.
17 Z. Liu, G. Ma, X. Zhu, Y. Shen, X. Guo, Y. Ding, J. Liu, D. Khalafallah, X. Huang, B. Guo and S. Li, *ACS Energy Lett.*, 2026, **11**, 1514–1537.
18 S. Li, Y. Pang, H. Li, R. Yang, Z. Jin, G. Yu and P. Li, *Chem. Sci.*, 2026, **17**, 772–790.
19 S. Wang, F. Li, J. Zhao, Y. Zeng, Y. Li, Z. Y. Lin, T. J. Lee, S. Liu, X. Ren, W. Wang, Y. Chen, S. F. Hung, Y. R. Lu, Y. Cui, X. Yang, X. Li, Y. Huang and B. Liu, *Nat. Commun.*, 2024, **15**, 10247.
20 X. Shi, Z. Wen, Q. Gu, L. Jiao, H.-L. Jiang, H. Lv, H. Wang, J. Ding, M. P. Lyons, A. Chang, Z. Feng, S. Chen, Y. Lin, X. Xu, P. Du, W. Xu, M. Sun, Y. Li, B. Yang, T. Zhang, X. Wu and J. Lu, *Nature*, 2025, **640**, 668–675.
21 L. Liu, J. Liu, G. Li, X. Shi, J. Yin, S. Zheng, K. F. Yung, H. B. Yang and T. W. B. Lo, *Angew. Chem., Int. Ed.*, 2025, **64**, e202422744.
22 H. Zhang, H. Han, L. Xiao and W. Wu, *ChemCatChem*, 2021, **13**, 3333–3339.
23 S. A. Chala, K. Lakshmanan, W.-H. Huang, A. W. Kahsay, C.-Y. Chang, F. T. Angerasa, Y.-F. Liao, J.-F. Lee, H. Dai, M.-C. Tsai, W.-N. Su and B. J. Hwang, *Appl. Catal., B*, 2024, **358**, 124420.
24 J. Zhu, M. Xiao, D. Ren, R. Gao, X. Liu, Z. Zhang, D. Luo, W. Xing, D. Su, A. Yu and Z. Chen, *J. Am. Chem. Soc.*, 2022, **144**, 9661–9671.
25 J. Toyir, P. R. r. de la Piscina, J. L. G. Fierro and N. s. Homs, *Appl. Catal., B*, 2001, **29**, 207–215.
26 C. B. Hiragond, N. S. Powar, J. Lee and S.-I. In, *Small*, 2022, **18**, 2201428.
27 Y. Han, C. Fang, X. Ji, J. Wei, Q. Ge and J. Sun, *ACS Catal.*, 2020, **10**, 12098–12108.

28 S. Wang, L. Wang, D. Wang and Y. Li, *Energy Environ. Sci.*, 2023, **16**, 2759–2803.
29 A. Ait El Fakir, P. Du, B. Yang, N. H. M. Dostagir, J. W. A. Fischer, A. Anzai, K. I. Shimizu and T. Toyao, *ChemSusChem*, 2025, **18**, e202500188.
30 X. Li, W. Song, K. Wang, Y. Jiang, W. Zhang, T. Liu, C. Huang, W. Qiang, X. Feng and J. Zhang, *Fuel*, 2026, **416**, 138593.
31 D. Xu, Y. Wang, M. Ding, X. Hong, G. Liu and S. C. E. Tsang, *Chem*, 2021, **7**, 849–881.
32 W.-Q. Li, J. M. Arce-Ramos, M. B. Sullivan, C. Kok Poh, L. Chen, A. Borgna and J. Zhang, *J. Catal.*, 2023, **421**, 185–193.
33 D. Xu, M. Ding, X. Hong, G. Liu and S. C. E. Tsang, *ACS Catal.*, 2020, **10**, 5250–5260.
34 K. Lee, H. Yan, Q. Sun, Z. Zhang and N. Yan, *Acc. Mater. Res.*, 2023, **4**, 746–757.
35 G. M. Landwehr, B. Vogeli, C. Tian, B. Singal, K. Zolkin, I. Martinez, A. Gupta, R. Lion, E. H. Sargent, A. S. Karim and M. C. Jewett, *Nat. Chem. Eng.*, 2025, **3**, 57–69.
36 M. K. Khan, S. Ahmed, S. S. Bibi, A. Helaley, X. Liang and J. Kim, *Chem. Eng. J.*, 2025, **517**, 164209.
37 L. Wang, L. Wang, J. Zhang, X. Liu, H. Wang, W. Zhang, Q. Yang, J. Ma, X. Dong, S. J. Yoo, J. G. Kim, X. Meng and F. S. Xiao, *Angew. Chem., Int. Ed.*, 2018, **57**, 6104–6108.
38 L. Wang, S. He, L. Wang, Y. Lei, X. Meng and F.-S. Xiao, *ACS Catal.*, 2019, **9**, 11335–11340.
39 X. Wang, P. J. Ramirez, W. Liao, J. A. Rodriguez and P. Liu, *J. Am. Chem. Soc.*, 2021, **143**, 13103–13112.
40 L. Ding, T. Shi, J. Gu, Y. Cui, Z. Zhang, C. Yang, T. Chen, M. Lin, P. Wang, N. Xue, L. Peng, X. Guo, Y. Zhu, Z. Chen and W. Ding, *Chem*, 2020, **6**, 2673–2689.
41 J. Chen, Y. Zha, B. Liu, Y. Li, Y. Xu and X. Liu, *ACS Catal.*, 2023, **13**, 7110–7121.
42 M. M. Yang, X. H. Bao and W. X. Li, *J. Chem. Phys.*, 2007, **127**, 024705.
43 Y. Deng, J. Zhao, S. Wang, R. Chen, J. Ding, H. J. Tsai, W. J. Zeng, S. F. Hung, W. Xu, J. Wang, F. Jaouen, X. Li, Y. Huang and B. Liu, *J. Am. Chem. Soc.*, 2023, **145**, 7242–7251.
44 K. Zheng, Y. Li, B. Liu, F. Jiang, Y. Xu and X. Liu, *Angew. Chem., Int. Ed.*, 2022, **61**, e202210991.
45 A. Wang, J. Li and T. Zhang, *Nat. Rev. Chem.*, 2018, **2**, 65–81.
46 J. Ren, N. Ai, D. Ou and Y. Yu, *Mol. Catal.*, 2023, **538**, 112990.
47 T. H. Pham, J. Cao, N. Song, Y. Cao, B. Chen, G. Qian, X. Zhou, D. Chen and X. Duan, *Green Energy Environ.*, 2022, **7**, 449–456.
48 N. J. Azhari, D. Erika, S. Mardiana, T. Ilmi, M. L. Gunawan, I. G. B. N. Makertihartha and G. T. M. Kadja, *Results Eng.*, 2022, **16**, 100711.
49 C. Zhou, A. Aitbekova, G. Liccardo, J. Oh, M. L. Stone, E. J. McShane, B. Werghi, S. Nathan, C. Song, J. Ciston, K. C. Bustillo, A. S. Hoffman, J. Hong, J. Perez-Aguilar, S. R. Bare and M. Cargnello, *Angew. Chem., Int. Ed.*, 2024, **63**, e202406761.
50 J. K. Norskov, T. Bligaard, J. Rossmeisl and C. H. Christensen, *Nat. Chem.*, 2009, **1**, 37–46.
51 S. Nitopi, E. Bertheussen, S. B. Scott, X. Liu, A. K. Engstfeld, S. Horch, B. Seger, I. E. L. Stephens, K. Chan, C. Hahn, J. K. Norskov, T. F. Jaramillo and I. Chorkendorff, *Chem. Rev.*, 2019, **119**, 7610–7672.
52 Y. Jiang, H. Guo, F. Cheng and Z.-X. Chen, *J. Phys. Chem. C*, 2025, **129**, 8096–8105.
53 F. Li, Y. C. Li, Z. Wang, J. Li, D.-H. Nam, Y. Lum, M. Luo, X. Wang, A. Ozden, S.-F. Hung, B. Chen, Y. Wang, J. Wicks, Y. Xu, Y. Li, C. M. Gabardo, C.-T. Dinh, Y. Wang, T.-T. Zhuang, D. Sinton and E. H. Sargent, *Nat. Catal.*, 2019, **3**, 75–82.
54 S. Li, L. Feng, H. Wang, Y. Lin, Z. Sun, L. Xu, Y. Xu, X. Liu, W. X. Li, S. Wei, J. X. Liu and J. Lu, *Nat. Nanotechnol.*, 2025, **20**, 255–264.
55 M. Z. Gu, Y. Min, L. Jiang, F. Zhou, Q. Chen, X. J. Zhang, J. J. Chen, H. Q. Yu and G. F. Wang, *Nat. Commun.*, 2025, **17**, 488.
56 X. Wang, Z. Wang, F. P. García de Arquer, C.-T. Dinh, A. Ozden, Y. C. Li, D.-H. Nam, J. Li, Y.-S. Liu, J. Wicks, Z. Chen, M. Chi, B. Chen, Y. Wang, J. Tam, J. Y. Howe, A. Proppe, P. Todorović, F. Li, T.-T. Zhuang, C. M. Gabardo, A. R. Kirmani, C. McCallum, S.-F. Hung, Y. Lum, M. Luo, Y. Min, A. Xu, C. P. O'Brien, B. Stephen, B. Sun, A. H. Ip, L. J. Richter, S. O. Kelley, D. Sinton and E. H. Sargent, *Nat. Energy*, 2020, **5**, 478–486.
57 C. Zhan, F. Dattila, C. Rettenmaier, A. Herzog, M. Herran, T. Wagner, F. Scholten, A. Bergmann, N. Lopez and B. Roldan Cuenya, *Nat. Energy*, 2024, **9**, 1485–1496.
58 P. Liu, N. Sun, J. Su, Y. Wang, Z. Peng, S. Chen, P. Papangelakis, A. Ozden, R. K. Miao, X. Wang, Y. Xu, J. Zeng, H. Wang, H. Liu, Y. Zhao, S. Shi, M. Shakouri, H. Liang, Z. Wang, H. Zhang, Y. Hu, Z. Yao, D. Sinton and J. Li, *Nat. Synth.*, 2025, **4**, 1462–1472.
59 J. Ding, H. Bin Yang, X.-L. Ma, S. Liu, W. Liu, Q. Mao, Y. Huang, J. Li, T. Zhang and B. Liu, *Nat. Energy*, 2023, **8**, 1386–1394.
60 H. Jin, K. Zhou, R. Zhang, H. Cui, Y. Yu, P. Cui, W. Song and C. Cao, *Nat. Commun.*, 2023, **14**, 2494.
61 Z. Li, P. Wang, X. Lyu, V. K. R. Kondapalli, S. Xiang, J. D. Jimenez, L. Ma, T. Ito, T. Zhang, J. Raj, Y. Fang, Y. Bai, J. Li, A. Serov, V. Shanov, A. I. Frenkel, S. D. Senanayake, S. Yang, T. P. Senftle and J. Wu, *Nat. Chem. Eng.*, 2024, **1**, 159–169.
62 Y. He, S. Liu, W. Fu, C. Wang, C. Mebrahtu, R. Sun and F. Zeng, *ACS Omega*, 2022, **7**, 16502–16514.
63 Y. Liu, X. Zhang, Z. Wang, J. Li, Q. Lv, D. Wang, S. Zhao, L. Wang, S. Zhang and Y. Pan, *Adv. Mater.*, 2026, **38**, e13175.
64 T. Zhang, A. G. Walsh, J. Yu and P. Zhang, *Chem. Soc. Rev.*, 2021, **50**, 569–588.
65 X. Ye, C. Yang, X. Pan, J. Ma, Y. Zhang, Y. Ren, X. Liu, L. Li and Y. Huang, *J. Am. Chem. Soc.*, 2020, **142**, 19001–19005.
66 K. Zheng, Y. Li, B. Liu, J. Chen, Y. Xu, Z. Li and X. Liu, *Appl. Catal., B*, 2024, **346**, 123730.

67 F. J. Caparrós, L. Soler, M. D. Rossell, I. Angurell, L. Piccolo, O. Rossell and J. Llorca, *ChemCatChem*, 2018, **10**, 2365–2369.
68 Y. Lou, F. jiang, W. Zhu, L. Wang, T. Yao, S. Wang, B. Yang, B. Yang, Y. Zhu and X. Liu, *Appl. Catal., B*, 2021, **291**, 120122.
69 Z. He, Q. Qian, J. Ma, Q. Meng, H. Zhou, J. Song, Z. Liu and B. Han, *Angew. Chem., Int. Ed.*, 2015, **128**, 747–751.
70 T. Yang, X. Mao, Y. Zhang, X. Wu, L. Wang, M. Chu, C. W. Pao, S. Yang, Y. Xu and X. Huang, *Nat. Commun.*, 2021, **12**, 6022.
71 B. An, Z. Li, Y. Song, J. Zhang, L. Zeng, C. Wang and W. Lin, *Nat. Catal.*, 2019, **2**, 709–717.
72 D. Wang, Q. Bi, G. Yin, W. Zhao, F. Huang, X. Xie and M. Jiang, *Chem. Commun.*, 2016, **52**, 14226–14229.
73 A. H. M. da Silva, L. H. Vieira, C. S. Santanta, M. T. M. Koper, E. M. Assaf, J. M. Assaf and J. F. Gomes, *Appl. Catal., B*, 2023, **324**, 122221.
74 H. Zhao, R. Yu, S. Ma, K. Xu, Y. Chen, K. Jiang, Y. Fang, C. Zhu, X. Liu, Y. Tang, L. Wu, Y. Wu, Q. Jiang, P. He, Z. Liu and L. Tan, *Nat. Catal.*, 2022, **5**, 818–831.
75 W. Wu, Y. Wang, L. Luo, M. Wang, Z. Li, Y. Chen, Z. Wang, J. Chai, Z. Cen, Y. Shi, J. Zhao, J. Zeng and H. Li, *Angew. Chem., Int. Ed.*, 2022, **61**, e202213024.
76 R. Ye, J. Ding, T. R. Reina, M. S. Duyar, H. Li, W. Luo, R. Zhang, M. Fan, G. Feng, J. Sun and J. Liu, *Nat. Synth.*, 2025, **4**, 288–302.
77 J. Pei, H. Shang, J. Mao, Z. Chen, R. Sui, X. Zhang, D. Zhou, Y. Wang, F. Zhang, W. Zhu, T. Wang, W. Chen and Z. Zhuang, *Nat. Commun.*, 2024, **15**, 416.
78 C. M. Zeng and J. A. Panetier, *Acc. Chem. Res.*, 2025, **58**, 342–353.
79 Z. Chen, Z. Liu and X. Xu, *Nat. Commun.*, 2023, **14**, 2512.
80 J. Hu, L. Yu, J. Deng, Y. Wang, K. Cheng, C. Ma, Q. Zhang, W. Wen, S. Yu, Y. Pan, J. Yang, H. Ma, F. Qi, Y. Wang, Y. Zheng, M. Chen, R. Huang, S. Zhang, Z. Zhao, J. Mao, X. Meng, Q. Ji, G. Hou, X. Han, X. Bao, Y. Wang and D. Deng, *Nat. Catal.*, 2021, **4**, 242–250.
81 F. Kraushofer and G. S. Parkinson, *Chem. Rev.*, 2022, **122**, 14911–14939.
82 G. S. Parkinson, Z. Novotny, G. Argentero, M. Schmid, J. Pavelec, R. Kosak, P. Blaha and U. Diebold, *Nat. Mater.*, 2013, **12**, 724–728.
83 L. X. Wang, L. Wang and F. S. Xiao, *Chem. Sci.*, 2021, **12**, 14660–14673.
84 J. Zhang, Y. Wang and Y. Li, *J. Am. Chem. Soc.*, 2024, **146**, 14954–14958.
85 R. Ye, L. Ma, J. Mao, X. Wang, X. Hong, A. Gallo, Y. Ma, W. Luo, B. Wang, R. Zhang, M. S. Duyar, Z. Jiang and J. Liu, *Nat. Commun.*, 2024, **15**, 2159.
86 S. Chen, *ChemSusChem*, 2025, **18**, e202401437.
87 W. Chu, Q. Zheng, O. V. Prezhdo and J. Zhao, *J. Am. Chem. Soc.*, 2020, **142**, 3214–3221.
88 F.-l. Sun, C.-b. Lin, W. Zhang, Q. Chen, W.-x. Chen, X.-n. Li and G.-l. Zhuang, *npj Comput. Mater.*, 2023, **9**, 220.
89 B. Qiao, A. Wang, X. Yang, L. F. Allard, Z. Jiang, Y. Cui, J. Liu, J. Li and T. Zhang, *Nat. Chem.*, 2011, **3**, 634–641.
90 Y. Chen, C. Zhang, D. Yao, O. M. Gazit and Z. Zhong, *ACS Appl. Mater. Interfaces*, 2025, **17**, 3404–3417.
91 Z. Li, W. Wu, M. Wang, Y. Wang, X. Ma, L. Luo, Y. Chen, K. Fan, Y. Pan, H. Li and J. Zeng, *Nat. Commun.*, 2022, **13**, 2396.
92 Y. Zhang, F. Chen, X. Yang, Y. Guo, X. Zhang, H. Dong, W. Wang, F. Lu, Z. Lu, H. Liu, H. Liu, Y. Xiao and Y. Cheng, *Nat. Commun.*, 2025, **16**, 1956.
93 J. Su, L. Yu, B. Han, F. Li, Z. Chen and X. C. Zeng, *J. Phys. Chem. Lett.*, 2024, **15**, 8600–8607.
94 M. Wang, Y. Xu, H. Tang, S. Tian, L. Zeng, H. Li, C. Wu, Z. Hu, M. Su, H. Zheng, M. Wang and D. Ma, *Chem Catal.*, 2024, **4**, 100985.
95 M. Yang, J. Yu, A. Zimina, B. B. Sarma, J.-D. Grunwaldt, H. Zada, L. Wang and J. Sun, *Angew. Chem., Int. Ed.*, 2024, **63**, e202312292.
96 W. Hua, X. Yang, Z. Zheng, M. Ma, K. Feng, D. Song, P. Liu, F. Lyu, J. Zhong, Z. Deng and Y. Peng, *J. Energy Chem.*, 2026, **114**, 277–286.
97 Q. Yang, H. Liu, Y. Lin, D. Su, Y. Tang and L. Chen, *Adv. Mater.*, 2024, **36**, e2310912.
98 W. Xia, Y. Xie, S. Jia, S. Han, R. Qi, T. Chen, X. Xing, T. Yao, D. Zhou, X. Dong, J. Zhai, J. Li, J. He, D. Jiang, Y. Yamauchi, M. He, H. Wu and B. Han, *J. Am. Chem. Soc.*, 2023, **145**, 17253–17264.
99 B. J. O'Neill, D. H. K. Jackson, J. Lee, C. Canlas, P. C. Stair, C. L. Marshall, J. W. Elam, T. F. Kuech, J. A. Dumesic and G. W. Huber, *ACS Catal.*, 2015, **5**, 1804–1825.
100 W. Li, Z. Guo, J. Yang, Y. Li, X. Sun, H. He, S. Li and J. Zhang, *Electrochem. Energy Rev.*, 2022, **5**, 9.
101 E. T. C. Vogt, D. Fu and B. M. Weckhuysen, *Angew. Chem., Int. Ed.*, 2023, **62**, e202300319.
102 L. He, C. Guan, D. A. Bulushev and Q. Xiang, *Small*, 2024, e2410976.
103 J. Liu, *ACS Catal.*, 2016, **7**, 34–59.
104 Z. K. Yu, M. Jiang, S. Dai, W. Zhan, Z. Q. Wang and X. Q. Gong, *Nat. Commun.*, 2025, **16**, 9072.
105 B. Rungtaweevoranit, J. Baek, J. R. Araujo, B. S. Archanjo, K. M. Choi, O. M. Yaghi and G. A. Somorjai, *Nano Lett.*, 2016, **16**, 7645–7649.
106 C. Zhong, Y. Yang, J. Chen, B. Feng, H. Wang and Y. Yao, *ACS Appl. Nano Mater.*, 2024, **7**, 14057–14068.
107 X. Cui, M. Luo, Z. Yang, R. Rahman, Z. Li, W. Yang and L. Xia, *Energy Fuels*, 2025, **39**, 2675–2687.
108 Z. Lang, X. Wang, S. Jabeen, Y. Cheng, N. Liu, Z. Liu, T. Gan, Z. Zhuang, H. Li and D. Wang, *Adv. Mater.*, 2025, **37**, e2418942.
109 Y. Pan, X. Zhang, G. Sun, Y. Li and B. Liu, *ACS Catal.*, 2025, **15**, 3674–3698.
110 R. J. P. Broos, B. Zijlstra, I. A. W. Filot and E. J. M. Hensen, *J. Phys. Chem. C*, 2018, **122**, 9929–9938.
111 B. Chen, D. Wang, X. Duan, W. Liu, Y. Li, G. Qian, W. Yuan, A. Holmen, X. Zhou and D. Chen, *ACS Catal.*, 2018, **8**, 2709–2714.
112 W. Gong, J. Ma, G. Chen, Y. Dai, R. Long, H. Zhao and Y. Xiong, *Chem. Soc. Rev.*, 2025, **54**, 960–982.

113 L. Zhang, S. Song, H. Zhang and X. Wang, *Chem. Soc. Rev.*, 2026, **55**, 504–555.
114 L. Song, G. Liu, X. Jiang and Z. Qu, *ACS Catal.*, 2025, **15**, 11243–11256.
115 L. Dawei, Z. Tianyu, G. Xiaoju, Y. Xiang, H. Aijuan and L. Junfeng, *Microstructures*, 2025, **5**, 2025023.
116 J. Feng, Y. He, Y. Liu, Y. Du and D. Li, *Chem. Soc. Rev.*, 2015, **44**, 5291–5319.
117 F. Wang, Y. Liu, M. Peng, M. Yang, Y. Chen, J. Du and A. Chen, *ACS Catal.*, 2024, **14**, 16434–16458.
118 Y. Xiang, S. Yin, Y. Su, Y. Chang, D. Guo, L. Wu, X. Chen and S. Wang, *ChemSusChem*, 2025, **18**, e202501163.
119 L. Gloag, S. V. Somerville, J. J. Gooding and R. D. Tilley, *Nat. Rev. Mater.*, 2024, **9**, 173–189.
120 Z. Chen, A. G. Walsh and P. Zhang, *Acc. Chem. Res.*, 2024, **57**, 521–532.
121 Y. Liu, X. Su, J. Ding, J. Zhou, Z. Liu, X. Wei, H. B. Yang and B. Liu, *Chem. Soc. Rev.*, 2024, **53**, 11850–11887.
122 S. A. Ali, I. Sadiq and T. Ahmad, *Chem. Commun.*, 2025, **61**, 8157–8169.
123 X.-F. Yang, A. Wang, B. Qiao, J. Li, J. Liu and T. Zhang, *Acc. Chem. Res.*, 2013, **46**, 1740–1748.
124 Y. Tang, H. Wang, C. Guo, L. Wang, T. Zhao, S. Xiao, J. Liu, Y. Jiang, Y. Zhao, X. D. Wen and F. Wang, *Adv. Mater.*, 2026, **38**, e12793.
125 S. Verma, M. Kumari, R. Maurya and K. Roy, *Mater. Today*, 2025, **89**, 606–620.
126 B. Liu, M. Li, X. Chen, Y. Sun, W. Wang, Z. Fan, X. Lan, F. Wei, B. Yan, Q. Zhong and T. Wang, *J. Am. Chem. Soc.*, 2025, **147**, 15859–15866.
127 H. Geng, H. Zhao, L. Yang, Z. Li, J. Ran and N. B. Li, *ACS Sustainable Chem. Eng.*, 2025, **13**, 7939–7948.
128 E. Kotob, M. M. Awad, M. Umar, O. A. Taialla, I. Hussain, S. I. Alsabbahen, K. Alhooshani and S. A. Ganiyu, *iScience*, 2025, **28**, 112306.
129 K. R. Lee, A. Jaleel, K. Park, S. Ahn, A. Haider, U. Lee and K.-D. Jung, *J. Catal.*, 2026, **453**, 116508.
130 N. Choudhary, K. Nabeela, N. Mate and S. M. Mobin, *RSC Sustainability*, 2024, **2**, 1179–1201.
131 M. A. Canovas, A. Gracia, R. Sayos and P. Gamallo, *J. Phys. Chem. C*, 2024, **128**, 16551–16562.
132 Q. M. Zhang, Z. Y. Wang, H. Zhang, X. H. Liu, W. Zhang and L. B. Zhao, *Phys. Chem. Chem. Phys.*, 2024, **26**, 11037–11047.
133 H. Sun and J.-y. Liu, *ACS Catal.*, 2024, **14**, 14021–14030.
134 G. Lin, T. Guo, W. Lin, H. Fan, L. Guo, Z. Zhang, B. Li, J. Wang, H. Ji, W. Song and J. Fu, *ACS Catal.*, 2025, **15**, 13534–13548.
135 L.-H. Mou, J. Du, Y. Li, J. Jiang and L. Chen, *ACS Catal.*, 2024, **14**, 12947–12955.
136 J. Chen, J. Li, X. Hai, J. Li, T. Zhang and J. Lu, *J. Am. Chem. Soc.*, 2025, **147**, 44617–44632.
137 X. Wen, X. Geng, G. Su, Y. Li, Q. Li, Y. Yi and L. Liu, *Green Chem.*, 2025, **27**, 4898–4925.
138 J. Benavides-Hernández and F. Dumeignil, *ACS Catal.*, 2024, **14**, 11749–11779.
139 S. Gul, F. Nasim and M. A. Nadeem, *ACS Appl. Energy Mater.*, 2025, **8**, 11786–11812.
140 A. H. Jenkins, E. E. Dunphy, M. F. Toney, C. B. Musgrave and J. W. Medlin, *ACS Catal.*, 2023, **13**, 15340–15350.
141 A. A. M. Abahussain, F. A. Nasr, A. S. Al-Fatesh, P. Sambandam, M. Al-zharani, F. A. A. Ali, N. Siva Kumar, S. A. Alsalamah, G. Subbiah, G. Loganathan, S. Palanivelu, S. Gunasekaran, K. Chandrasekaran and T. Perumal, *Green Chem.*, 2025, **27**, 11607–11655.
142 L. Zhang, M. N. Banis and X. Sun, *Natl. Sci. Rev.*, 2018, **5**, 628–630.
143 J. Fonseca and J. Lu, *ACS Catal.*, 2021, **11**, 7018–7059.
144 N. Cheng and X. Sun, *Chin. J. Catal.*, 2017, **38**, 1508–1514.
145 N. Cheng, L. Zhang, K. Doyle-Davis and X. Sun, *Electrochem. Energy Rev.*, 2019, **2**, 539–573.
146 H. Wang, C. Gong, X. Xin, S. Li, J. Zhang, B. Ye, X. Bu, J. Li and P. Gao, *Angew. Chem., Int. Ed.*, 2025, **64**, e202516545.
147 L. Zhang, R. Si, H. Liu, N. Chen, Q. Wang, K. Adair, Z. Wang, J. Chen, Z. Song, J. Li, M. N. Banis, R. Li, T. K. Sham, M. Gu, L. M. Liu, G. A. Botton and X. Sun, *Nat. Commun.*, 2019, **10**, 4936.
148 H. Yan, H. Cheng, H. Yi, Y. Lin, T. Yao, C. Wang, J. Li, S. Wei and J. Lu, *J. Am. Chem. Soc.*, 2015, **137**, 10484–10487.
149 S. M. George, *Chem. Rev.*, 2010, **110**, 111–131.
150 K. Jiang, X.-Y. Ma, S. Back, J. Zhao, F. Jiang, X. Qin, J. Zhang and W.-B. Cai, *CCS Chem.*, 2021, **3**, 241–251.
151 S. Zou, Y. Liang, X. Zhang, Q. Gu, L. Wang, H. Sun, X. Liao, J. Huang and A. R. Masri, *Angew. Chem., Int. Ed.*, 2025, **64**, e202412835.
152 F. Liu, Y. Xia, W. Xu, L. Cao, Q. Guan, Q. Gu, B. Yang and J. Lu, *Angew. Chem., Int. Ed.*, 2021, **60**, 19324–19330.
153 O. S. Mendoza-Hernandez, A. Shima, H. Matsumoto, M. Inoue, T. Abe, Y. Matsuzaki and Y. Sone, *Sci. Rep.*, 2019, **9**, 6470.
154 K. Yang, M. Li, T. Gao, G. Xu, D. Li, Y. Zheng, Q. Li and J. Duan, *Nat. Commun.*, 2024, **15**, 7060.
155 J. Wang, J. Yang, Y. Feng, J. Hua, Z. Chen, M. Liao, J. Zhang and J. Qin, *Appl. Energy*, 2025, **379**, 124936.
156 A. Tan, J. Song, X. Qiu, Z. Liu, L. Xia, C. Ju, F. Zhao, G. Li, X. Shi, T. Li, P. Liu and J. Liu, *Nat. Commun.*, 2025, **16**, 9115.
157 S. Bai, X. Gu, J. Dong, J. Yang, W. Zheng, C. Guo, Y. Liu, T. Kong and S. Shen, *Adv. Energy Mater.*, 2026, e06790.
158 H. Gao, Y. Jiang, R. Chen, C. L. Dong, Y. C. Huang, M. Ma, Z. Shi, J. Liu, Z. Zhang, M. Qiu, T. Wu, J. Wang, Y. Jiang, J. Chen, X. An, Y. He and S. Wang, *Adv. Funct. Mater.*, 2023, **33**, 2214795.
159 D. Park, S. Hong, J. Han, Y. Kim, M. Park, B. Lee, Y. Song, H. Y. Koo, S. Yang, W. B. Lee and J. Y. Park, *Appl. Catal., B*, 2025, **365**, 124987.
160 F. Qureshi, M. Asif, A. Khan, A. Husain, H. Aldawsari, M. Yusuf, S. K. Verma and M. Y. Khan, *Int. J. Hydrogen Energy*, 2025, **141**, 954–978.
161 L. Yu, M. Ning, Y. Wang, C. Yuan and Z. Ren, *Nat. Rev. Mater.*, 2025, **10**, 857–873.
162 H. P. Tran, H. N. Nong, M. Zlatar, A. Yoon, U. Hejral, M. Ruscher, J. Timoshenko, S. Selve, D. Berger, M. Kroschel, M. Klingenhof, B. Paul, S. Mohle, K. N. Nagi Nasralla, D. Escalera-Lopez, A. Bergmann, S. Cherevko,

B. R. Cuenya and P. Strasser, *J. Am. Chem. Soc.*, 2024, **146**, 31444–31455.
163 C.-W. Tung, W. Zhang, T. Y. Lai, J. Wang, Y.-C. Chu, G.-B. Wang, C.-S. Hsu, Y.-F. Liao, N. Hiraoka, H. Ishii, X. C. Zeng and H. M. Chen, *Nat. Sustain.*, 2025, **8**, 793–805.
164 S. Ding, M. J. Hülsey, J. Pérez-Ramírez and N. Yan, *Joule*, 2019, **3**, 2897–2929.
165 N. Zou, J. Chen, T. Qiu and Y. Zheng, *J. Mater. Chem. A*, 2023, **11**, 10766–10775.
166 X. He, H. Zhang, X. Zhang, Y. Zhang, Q. He, H. Chen, Y. Cheng, M. Peng, X. Qin, H. Ji and D. Ma, *Nat. Commun.*, 2022, **13**, 5721.
167 M. R. Rahimpour, M. H. Khademi and A. M. Bahmanpour, *Chem. Eng. Sci.*, 2010, **65**, 6206–6214.